2015

Instituto Politécnico de Coimbra

INSTITUTO SUPERIOR DE ENGENHARIA DE COIMBRA

A new method for non-intrusive online wiring health monitoring

MESTRADO EM ENGENHARIA ELETROTÉCNICA

AUTOR | Alexandre dos Santos Martins

ORIENTADOR | Doutor João Paulo Morais Ferreira

Coimbra, julho 2015

Instituto Superior de
Engenharia de Coimbra

Departamento
de Engenharia Eletrotécnica

A new method for non-intrusive online wiring health monitoring

Relatório de Estágio apresentado para a obtenção do grau de Mestre em Engenharia Eletrotécnica – Área de Especialização em Automação e Comunicações em Sistemas Industriais

Autor
Alexandre dos Santos Martins

Orientador
Doutor João Paulo Morais Ferreira
Instituto Superior de Engenharia de Coimbra

Supervisor na Empresa
Engenheiro Alexandre Miguel Lopes Ribeiro
Active Space Technologies

Coimbra, julho, 2015

Acknowlegments

I would like to thank to everyone involved in the development of this project.

I am grateful to my advisors, PhD João Ferreira from Instituto Superior de Engenharia de Coimbra and Eng. Alexandre Ribeiro from Active Space Technologies, who have supported me with their knowledge throughout my internship.

I would like to thank to Eng. Abel Mendes and Fernando Simões from Active Space Technologies for all the insight during the development of this project.

I would like to express my gratitude to my colleagues from Active Space Technologies for the all the contributions and opinions.

I owe my deepest gratitude to my parents, Adília and António, my brother Nico, my girlfriend Filipa and my good friend Nuno for all the endless support.

Abstract

This work presents a method for preventing faults in cables prior to their happening, e.g. due to wire ageing and mounting fixtures. The proposed method focus in large diameter cables delivering high currents in aircraft. However, this method could be useful in other scenarios where wiring problems could cause critical problems such as in nuclear power plants, automobiles or trains.

The method consists of a sensor embedded in the cable. The sensor is made of several thin wires wrapped around the insulator of the monitoring cable in a mesh grid pattern.

The cable with the embedded sensor is then covered with a second layer of insulation. Measuring the equivalent resistance of the sensor, allows to determine the health of the cable, as a fault would also damage the sensor changing its equivalent resistance. Chafing faults, e.g. caused by wires rubbing against each other or bare wiring contact to ground or with the chassis of the vehicle, are analysed. The sensor equivalent resistance for each type of fault and its distance from the measurement system is characterized, enabling localization and prevention of wiring malfunctions.

A complete prototype of the system is described, including the hardware and software components of the sensor.

Additionally, the system is tested to verify operation in a environment similar to the one experienced in an aircraft.

This work was developed as part of an internship in the company Active Space Technologies.

Resumo

Este trabalho apresenta um novo método de predição de defeitos em cabos. Estes defeitos são provocados por processos de envelhecimento da instalação. O método tem especial utilidade na monitorização de cabos de elevado diâmetro transmitindo correntes elevadas no interior de aeronaves. Adicionalmente, este método também poderá ser útil na monitorização de cablagem em centrais nucleares, automóveis ou comboios.

O método consiste num sensor embebido na própria construção da cablagem. O sensor é constituído por um conjunto de elétrodos finos adequadamente distribuídos em forma de grelha, enrolados em torno do cabo a monitorizar. Uma segunda camada de isolamento é colocada em torno do conjunto.

Se ocorrer algum dano no sensor a sua resistência equivalente irá alterar-se. Medindo a resistência equivalente do sensor é possível determinar a saúde do cabo, pois danos no cabo também provocam danos no sensor. Danos causados pelo atrito entre cabos ou apoios de montagem, bem como falhas causadas pelo contato elétrico entre o cabo e o chassis do veículo ou sistema de terra, foram consideradas. A relação entre a resistência equivalente para cada tipo de falhas e sua distância ao sistema de medida foi estabelecida, permitindo a prevenção e localização de falhas. Um protótipo completo do sistema é descrito, incluindo o sensor e respetivo sistema de medição, contemplando o hardware e software desenvolvidos.

Adicionalmente, o sistema é testado para verificar a sua operacionalidade num ambiente não controlado similar ao existente numa aeronave.

Todo o trabalho foi desenvolvido como parte de um estágio curricular na empresa Active Space Technologies.

Contents

List of Figures

List of Tables

Abbreviations

ADC Analogue-to-Digital Converter

AES Advanced Encryption Standard

ATSRAC Aging Transport Systems Rulemaking Advisory Committee

CMOS Complementary Metal–Oxide–Semiconductor

CPU Central Processing Unit

CWT Center Wing fuel Tank

DAC Digital-to-Analogue Converter

DoD Department of Defense

EMC Electromagnetic Compatibility

FAA Federal Aviation Administration

FET Field-Effect Transistor

IC Integrated Circuit

ICAO International Civil Aviation Organization

INL Integral Non-Linearity

LCD Liquid-Crystal Display

NA Not Applicable

NASA National Aeronautics and Space Administration

NiCr Nickel-Chromium

OTP One-Time Programmable

PA Power Amplifier

PCB Printed Circuit Board

PVC Polyvinyl chloride

QPSK Quadrature Phase-Shift Keying

RAM Random-Access Memory

RF Radio Frequency

RISC Reduced Instruction Set Computer

ROM Read-Only Memory

RPK Revenue Passenger Kilometers

RTCA Radio Technical Commission for Aeronautics

RTOS Real-time Operating System

SAR Successive-Approximation Register

SMD Surface Mount Device

SMT Surface Mount Technology

SPI Serial Peripheral Interface

TDR Time-Domain Reflectometry

UART Universal Asynchronous Receiver/Transmitter

XTAL informal abbreviation for crystal

Chapter 1

Introduction

This chapter presents the motivation behind the developed work. In addition, the background of the work, objectives and defined workplan are presented. Finally, the outline of the document is shown.

1.1 Motivation

In this section, a brief market analysis is performed and the driving force behind the research for new methods of wiring health monitoring is presented.

1.1.1 Market

Air traffic has been increasing since the very beginning of aviation. This reflects the importance people give to the ability of reaching distant places in a short period of time to conduct business, visit family or go on holiday. As shown in Figure 1.1 air traffic has doubled every 15 years and it is expected that this trend will continue in the next 15 years. Over 2.9 billion people used air transport in 2012 and according to current predictions it is expected to reach over 6 billion users by 2030 [10].

In parallel with the grow of air transportation, air manufacturers struggle to increase reliability of aircraft, since airplane updating rather than replacement became a standard way of saving money [11]. Therefore, the average age of operating aircraft is increasing. In the United States of America the average age of aircraft have increased from 11.3 years in 2005 to 13.3 years in 2011 [12], representing a 17.7% increase.

The age of retirement of aircraft has increased significantly for the past decades, as shown in Figure 1.2. The average age of permanent withdrawal from use was 25.6 years in 2012 [2]. Further steps are being taken in order to continue increasing longevity, as one of the goals of the Federal Aviation Administration (FAA) is to improve reliability to reach 1 million flight hours of life expectancy.

The increased age of operating aircraft lead to increasing of ageing malfunctions. These ageing malfunctions begin to occur in every system of aircraft, including systems

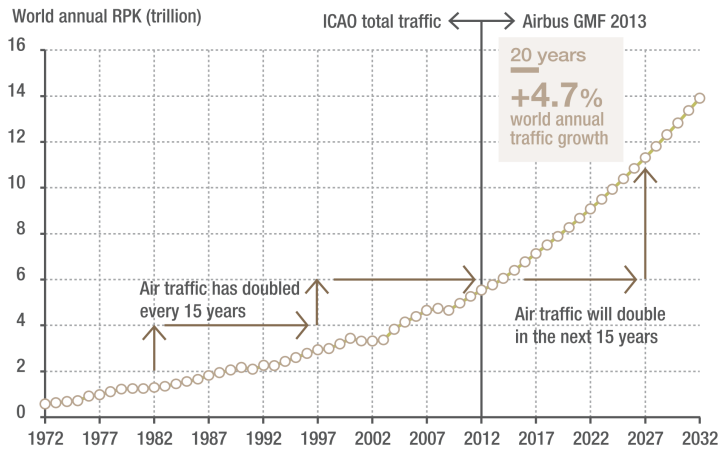

Figure 1.1: World annual Revenue Passenger Kilometers (RPK) history and previsions [1].

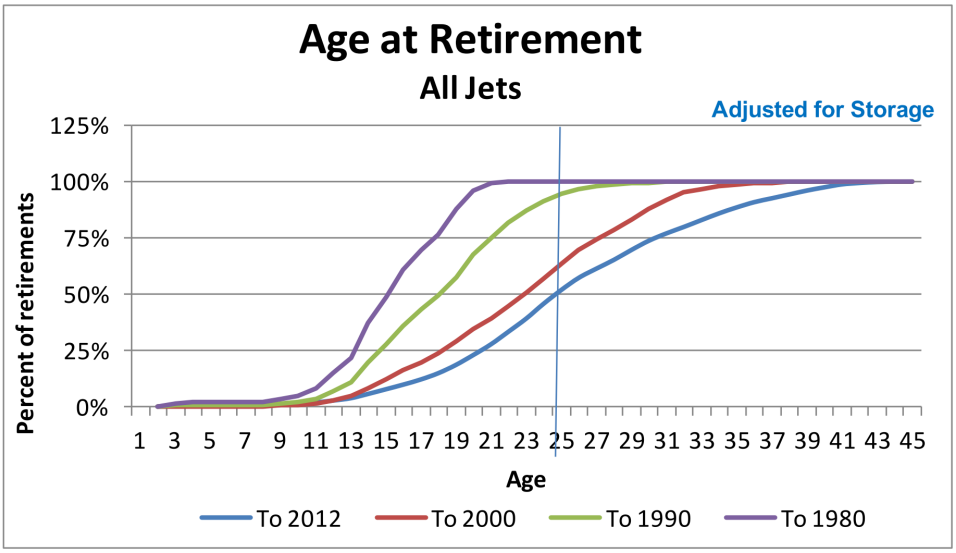

Figure 1.2: Age of retirement cumulative distribution [2].

considered benign and with large life cycle, namely electrical wiring. Once treated as a fit and forget system, wiring must now be considered a critical system with specific maintenance plan.

1.1.2 Wiring ageing

Wiring ageing is caused by accumulated damage from exposure to the following stresses:

- Chemical, including corrosion and moisture;
- Thermal;
- Electrical discharging;
- Mechanical, including vibration, chafing overload and fatigue;
- Radiological.

Wire systems are exposed to the stresses induced by the environment as well as poor installation and maintenance practices. An intrusive inspection performed by the Aging Transport Systems Rulemaking Advisory Committee (ATSRAC) on ageing aircraft revealed wire deterioration in several zones of the aircraft. Results from this intrusive inspection are shown in Figure 1.3, with over half of the deterioration conditions detected on wiring being mechanical by nature.

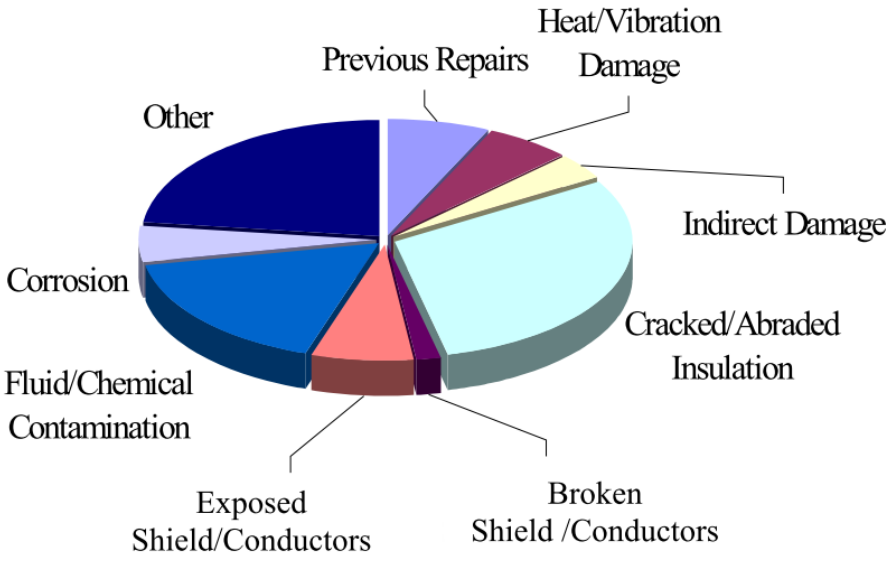

Figure 1.3: Wiring conditions from ATSRAC intrusive inspection. [3].

Wiring malfunctions can be as critical as any other system fault. A Boeing study from 1992 to 2000, whose data is shown in Figure 1.4, reports that most in-flight fires where originated by electrical problems [4]. From those events, wiring failures were among the higher rate of occurrence. Furthermore, wiring failures are one of the most difficult to troubleshoot, as wiring lies mostly buried inside the aircraft fuselage.

1.1.3 Accidents

On 17 July 1996, a Boeing 747-100 from Trans World Airlines (TWA800) exploded and crashed in the Atlantic Ocean 12 minutes after take-off from JFK International Airport on a passenger flight to Rome. All 230 people on board perished.

The United States of America National Transportation Safety Board has conducted an investigation after the accident and determined that the most probable cause was an explosion in the Center Wing fuel Tank (CWT), resulting from an ignition of the flammable fuel/air mixture in the tank. The investigation also determined that the source of ignition was likely a short circuit [13].

This accident has contributed to drive attention to wire condition in aircraft and recognized wiring systems as an issue of national concern in the United States of America. On 1997, the White House Commission for Aviation Safety and Security identified

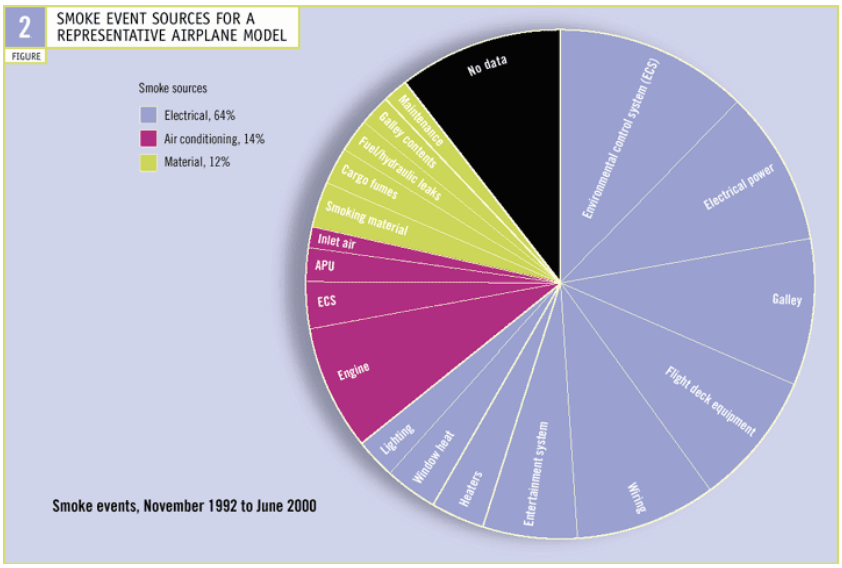

Figure 1.4: Smoke events by source type [4].

ageing wiring as a safety issue in aviation [14]. This commission recommended that three federal agencies – the Federal Aviation Administration (FAA), the Department of Defense (DoD), and the National Aeronautics and Space Administration (NASA) – expanded their ageing aircraft program to include the issue of ageing wire systems in commercial aviation.

On 2 September 1998, a McDonnell Douglas MD-11 from Swissair (SWR111) crashed in the Atlantic Ocean on a passenger flight from JFK International Airport to Geneva. All 229 people on board were killed. The most probable cause of the accident was an in-flight fire leading to electrical failure. The fire most likely started from a wire arcing event [15].

1.2 Background

Prior to the development of the present project, Active Space Technologies submitted a proposal [16] to CleanSky call for proposal on harness integrated sensor networks for wiring health monitoring [17]. The call focused on chafing detection in cables of large diameter (about 10 mm), delivering high power. Chafing can be defined as localized damage to the insulation and shielding of a wire, typically caused by wire rubbing over long periods of time against each other or their fixtures. Faulty wiring caused by chafing is shown in Figure 1.5.

Following the proposal, Active Space Technologies filed in a patent for a new method and system of monitoring electrical wire ageing [18]. The invention uses a set of thin electrodes wrapped around the insulating layer of the cable in a mesh shape. Deterioration of the insulation layer and of the electrodes can be subjected to real-time measurements, in order to predict the location of imminent insulation breakdown.

Figure 1.5: Chafed wire.

The present document reflects the work developed after the proposal and patent have been submitted by Active Space Technologies.

1.3 Objectives

The main goal of the project is to develop and test a fully functional prototype of a wiring health monitoring sensor and respective measurement unit.

The most important developments expected are:

- Study the proposed method and explore possible alternatives;
- Simulate and evaluate different topologies for the sensor structure, as well as the use of different materials;
- Develop a measurement system with user interface;
- Develop and conduct tests to evaluate the more critical aspects of the sensor.

1.4 Workplan

The work plan of the internship was divided into four phases. The defined timeline of the work plan is shown in Figure 1.6.

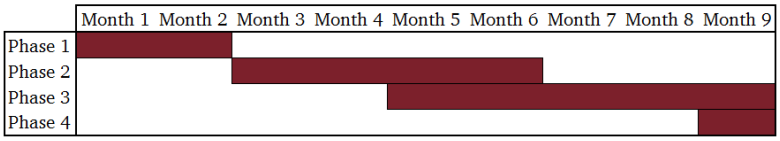

Figure 1.6: Defined timeline of the work plan.

Phase 1:

- Patent study.
- General definition of project goals.
- Evaluate different materials for sensor manufacturing.

- Analysis and validation of the concepts described in the patent.

Phase 2:

- Sensor requirements specification.
- Analog and digital circuit design of the measurement system.
- User interface definition.

Phase 3:

- Development of firmware for the measurement system.
- System integration.
- System testing and validation.

Phase 4:

- Report writing.

1.5 Outline

The outline of the presented document is as follows:

In Chapter 2 a brief overview of the current methods of wiring health assessment is presented.

In Chapter 3 is presented the rationale used to define the structure of the sensor.

In Chapter 4 is presented the measurement system architecture and the operation of its subsystems. In addition, a detailed analysis of the electronics and software is performed.

In Chapter 5 the specified test plan is presented along with results for the most critical test procedures.

In Chapter 6 are summarized the requirements that were met as well as subsequent work.

Chapter 2

State of the art

This chapter presents a brief overview about the methods currently used to assess the condition of wiring.

Several methods for wiring condition assessment exist, from visual inspection - with varying results depending on the experience of the technician - to tests performed in laboratory, enabling detailed analysis of the test specimen [19]. A list of several methods is shown in Table 2.1.

Table 2.1: Methods for fault detection in wiring and associated characteristics [16].

Technique	Skin Depth	Device Type	Method	Range	Live	Assessed Material
Time Domain Reflectometry	Surface	Electrical	Active	Global	Yes	Metal
Frequency Domain Reflectometry	surface	Electrical	Active	Global	?	Metal
Noise-Domain Reflectometry	Surface	Electrical	Passive	Global	Yes	Metal
Spread Spectrum Time Domain Reflectometry	Surface	Electrical	Active	Global	Yes	Metal
Inductance	Surface	Electrical	Passive	Local	?	Metal
Mutual Inductance	Surface	Electrical	Active	Local	Yes	Metal
Impedance	Surface	Electrical	Passive	Local	Yes	Metal and insulator*
Mutual Impedance	Surface	Electrical	Active	Local	?	?
Photometry	Surface	Optical	Passive	Local	Yes	Insulator
Acoustic Pulse Reflectometry	Bulk	Acoustic	Active	Global	Yes	Metal and insulator
Acoustic Transmission Line	Bulk	Acoustic	Active	Global	Yes	Metal and insulator

Most methods that can estimate the condition of a complete wiring set, including branches with only access to a section of the wiring, are based on Time-Domain Reflectrometry (TDR). Among those, only a small selection can be implemented in live wiring without disconnecting the cable to be monitored.

TDR is a measurement technique that uses reflected waveforms to identify discontinuities into an electrical line. In a transmission line as shown in Figure 2.1, if the load impedance Z_L is equal to the line impedance Z_0 all the energy from the generator V_S is absorbed in the load.

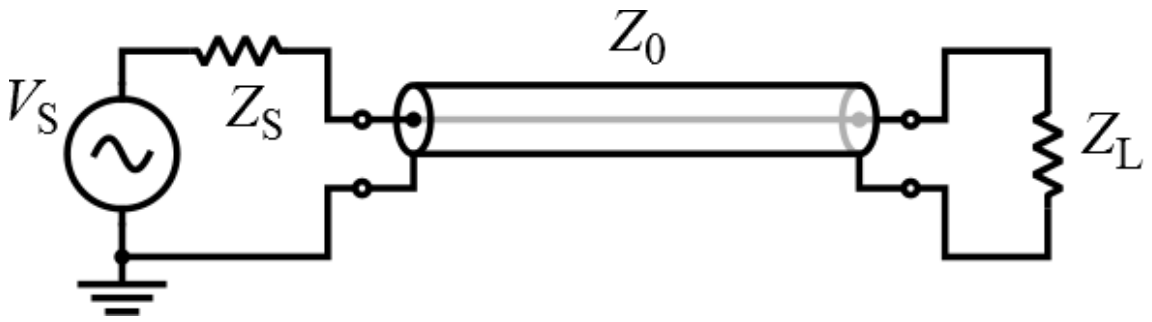

Figure 2.1: Transmission line [5].

If Z_L and Z_0 are different a second wave propagates back to the source when the first wave reaches the load. The ratio of mismatch between the load and line impedance gives the voltage reflection coefficient

$$\rho = \frac{E_R}{E_I} = \frac{Z_L - Z_0}{Z_L + Z_0}, \tag{2.1}$$

where E_I is the incident voltage and E_R is the reflected voltage.

Different faults in the transmission line generate different signatures in the reflected signal depending on the type of condition: open, short or partially open. Figure 2.2 shows different types of loads with respective reflected signals.

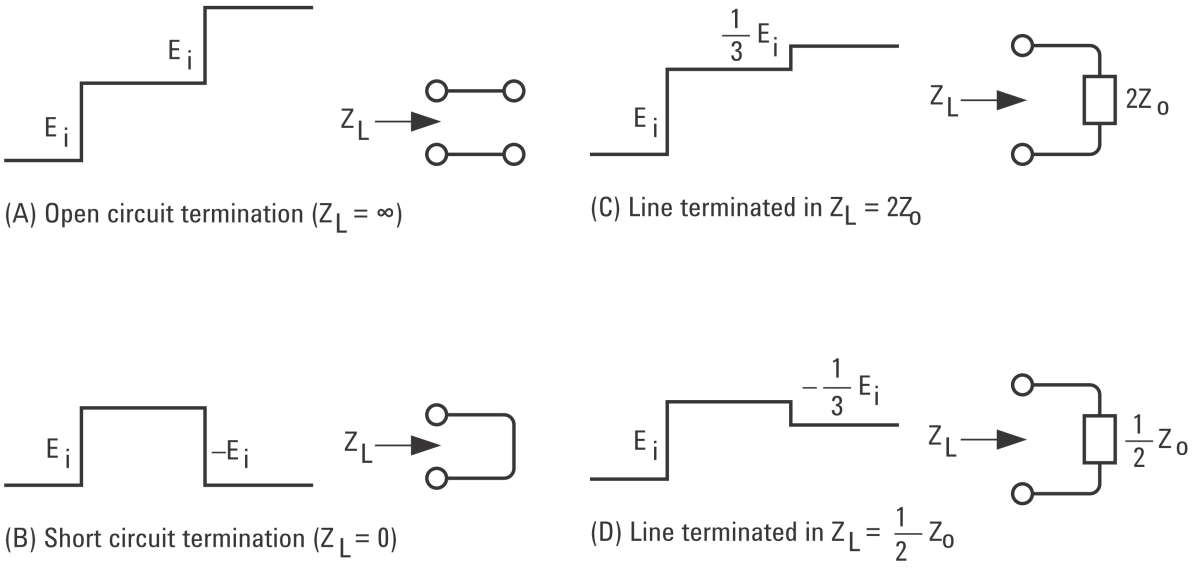

Figure 2.2: TDR displays for typical loads [6].

Also, the distance from impedance discontinuities can be calculated using

$$D = \frac{v_\rho T}{2} \tag{2.2}$$

where v_ρ is the velocity of propagation in the medium and T is the time of flight of the signal (injection-reflection-detection).

Alternatives to TDR techniques include assessment with Frequency Domain Reflectometry (FDR), Sequence Time Domain Reflectometry (STDR) and Spread-Spectrum Time Domain Reflectometry (SSTDR), whose responses are shown in Figure 2.3. These techniques improve the classic time domain method increasing accuracy and achieving better performance while operating in live wiring [7].

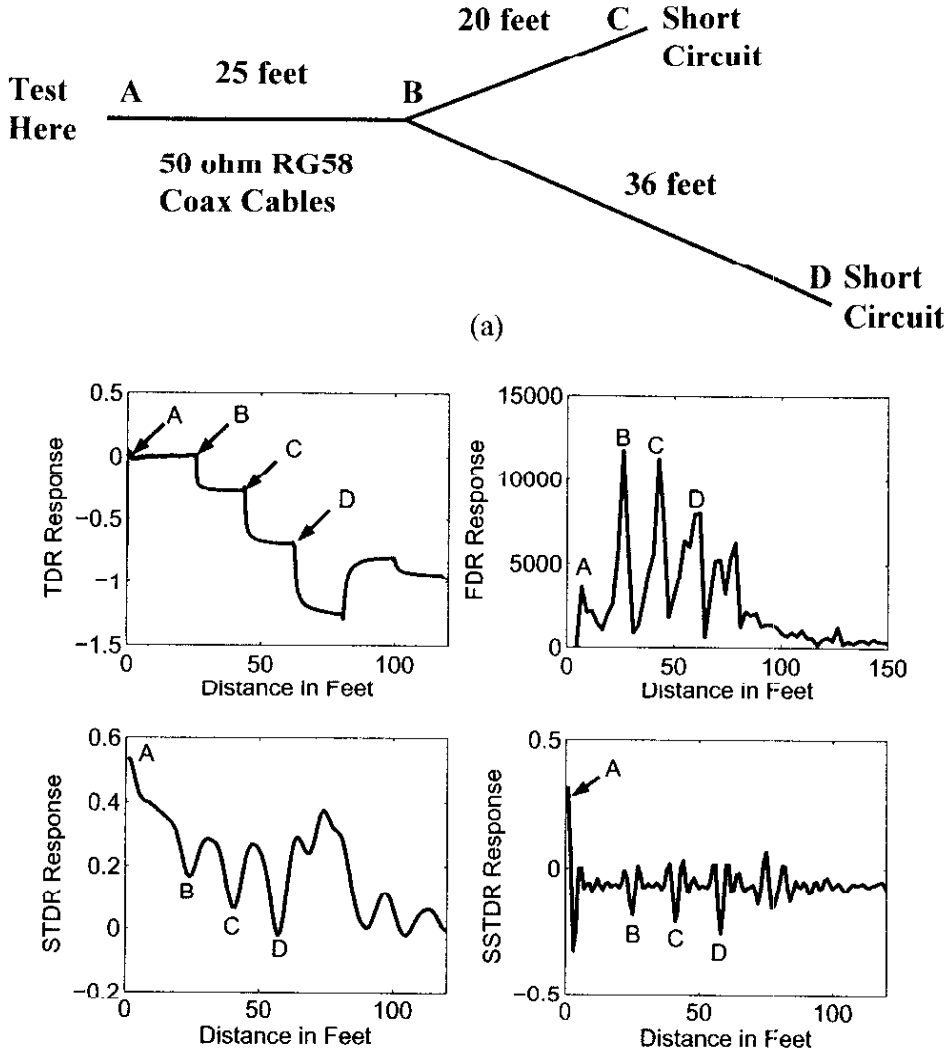

Figure 2.3: Tested network and reflected signals for different techniques of reflectrometry [7].

In a process similar to TDR methods, acoustic reflectrometry methods use the reflection of acoustic waves to detect possible faults in wiring. A proposed system using acoustic methods uses a pair of transducers separated by a certain distance and fixed to the wire to be monitored. Detection of faults can be achieved by analysis of the spectral signatures of the transmitted signal by each of the transducers, as they can be configured both as transmitter and receiver [20].

Capacitive and inductive sensors that measure the capacitance and inductance of wiring can detect the distance of open and short circuits. However, these sensors cannot locate faults in branched wires. Moreover, the inductance and capacitance of unshielded

or untwisted wires to be monitored change if they are close to metallic objects, namely other wires. [21].

One of the most common methods for wiring health assessment is the impedance method. This method is implemented by injecting a high voltage signal through the wire. This technique identifies degraded insulation by measuring the leakage current flowing through adjacent cables [20].

Not directly related to wiring health monitoring, but equally important, is the assessment of proper installation of wire harness clamps. An improper installation of a harness clamp can pinch a wire between the clamp ends possibly resulting in a premature failure of the wiring. Also, loose clamps can cause chafing, as small displacements of the wires are generated by aircraft vibration. There are proposed systems that include embedded sensors into the clamps to detect their proper installation [22].

Chapter 3

Sensor design

In this chapter is presented the rationale to define the structure of the sensor. It is discussed theoretical aspects of sensor performance and idealized model, as well as practical considerations derived from electrical and mechanical properties of the materials used. Finally, it is presented the prototype sensor built for proof-of-concept and validation purposes.

3.1 Sensor requirements

Initially, the requirements for the sensor to be simulated and built were defined. These requirements must be met in order to demonstrate the proof-of-concept.

- The sensor must detect defects with a 1 m resolution in long harness with a minimum diameter of 1 cm;
- Length of the monitoring unit should be at least 20 m;
- The sensor should be lightweight;
- The sensor should withstand adverse environment conditions during operation.

3.2 Sensor architecture

The sensor, as described in the patent, uses a set of thin insulated wires in a mesh pattern around the insulator of the main conductor or multiconductor to be monitored, as described in Figure 3.1. The protective mesh is wrapped around the conductor to be measured. The winding pitch defines the spatial resolution of the sensor, i.e., the shortest faulty segment the sensor can detect. There are also periodic connections from the protective mesh to a common wire. These connections are not depicted because they can vary according to the chosen sensor architecture.

The thin wires are arranged in a way that the equivalent resistance of the network measured from an edge characterizes the health of the main conductor indicating faults prior to their occurrence. Faults include cut of the protective mesh or contact of the

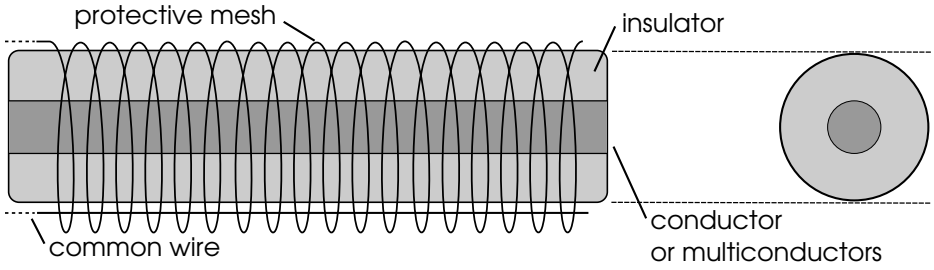

Figure 3.1: Simplified diagram of the sensor.

protective mesh to chassis or ground. The mesh pattern includes a periodic connection to a common wire along the length of the main conductor. This pattern creates elements that are in parallel with each other. Only with this kind of architecture is possible to detect and locate faults as each segment contributes to the total impedance of the sensor.

The structure can be modelled as a chain of resistors, as illustrated in Figure 3.2, because only the resistance is measured, thus the associated capacitance and inductance of the wires can be neglected. A series and parallel element form each mesh.

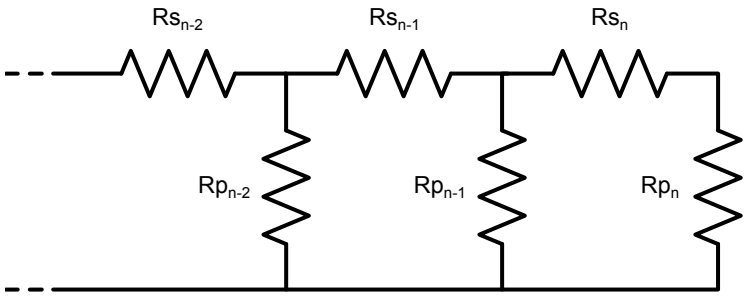

Figure 3.2: Equivalent circuit of the sensor with n meshes.

The equivalent resistance of the network can be obtained from

$$Req(i) = \begin{cases} Rs_n + Rp_n & , i = 1 \\ (Rp_i \parallel Req_{i+1}) + Rs_i & , i = 2, 3, ..., n \end{cases} \tag{3.1}$$

where Rs is the series resistance, Rp is the parallel resistance, n the number of meshes in the network and i is the index of the mesh in the network.

Since

$$Rp_i \parallel Req_{i+1} \quad = \quad \frac{Rp_i Req_{i+1}}{Rp_i + Req_{i+1}} \tag{3.2}$$

Equation 3.1 can be rewritten as

$$Req(i) = \begin{cases} Rs_n + Rp_n & , i = 1 \\ \dfrac{Rp_i Req_{i+1}}{Rp_i + Req_{i+1}} + Rs_i & , i = 2, 3, ..., n \end{cases} \tag{3.3}$$

3.2.1 Protective mesh

Based upon the defined requirements, two types of architecture can be considered. In one architecture, the protective mesh is composed by the elements in series and in the other architecture the protective mesh is composed by the elements in parallel. In both types of architecture, the elements that to not form the protective mesh, hereinafter referred to as offset elements, lie underneath the protective mesh, preventing faults on those elements.

A) Parallel Protective Mesh

In this architecture the parallel elements compose the protective mesh, as shown in Figure 3.3; the gap between windings is exaggerated. In fact, windings are close to each other and without gaps. The protective mesh is made of a winding with one terminal soldered to the positive wire and the other terminal soldered to the common wire. In this architecture, the series wire segments form the offset elements. The resistance of these segments defines the value of the series resistors in the equivalent circuit (Figure 3.2). The resistance of the winding defines the value of the parallel resistors.

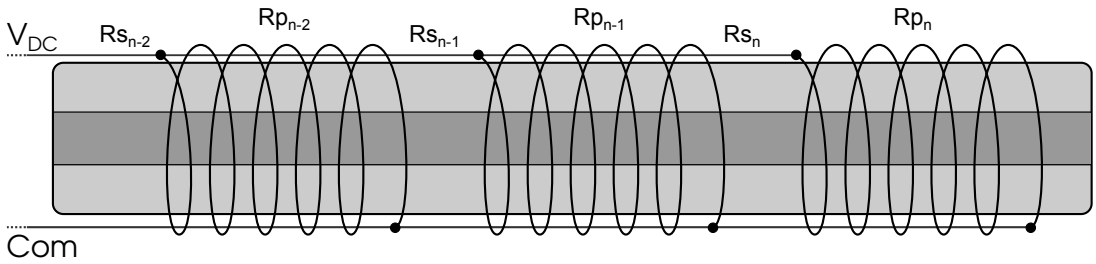

Figure 3.3: Diagram of sensor architecture using the protective mesh as the parallel element.

The equivalent circuit can be modified to represent the two types of faults as shown in Figure 3.4. When detecting faults using the protective mesh in parallel, a cut fault resulting for example from chafing can be represented by an open circuit in the affected element. Moreover, if a certain mesh of the network connects to the ground, that can be modelled as a variable resistor replacing that element. The value of this resistor is proportional to the distance to the leftmost solder joint of the winding where the fault happened and can possess values between 0 and Rp_i.

B) Series Protective Mesh

In this architecture the series elements compose the protective mesh, as shown in Figure 3.5. A series winding and a parallel segment (pictured as a resistor) form a mesh. The winding that forms the protective mesh is also the positive common wire. In this architecture the parallel wire segments or discrete resistors form the offset elements.

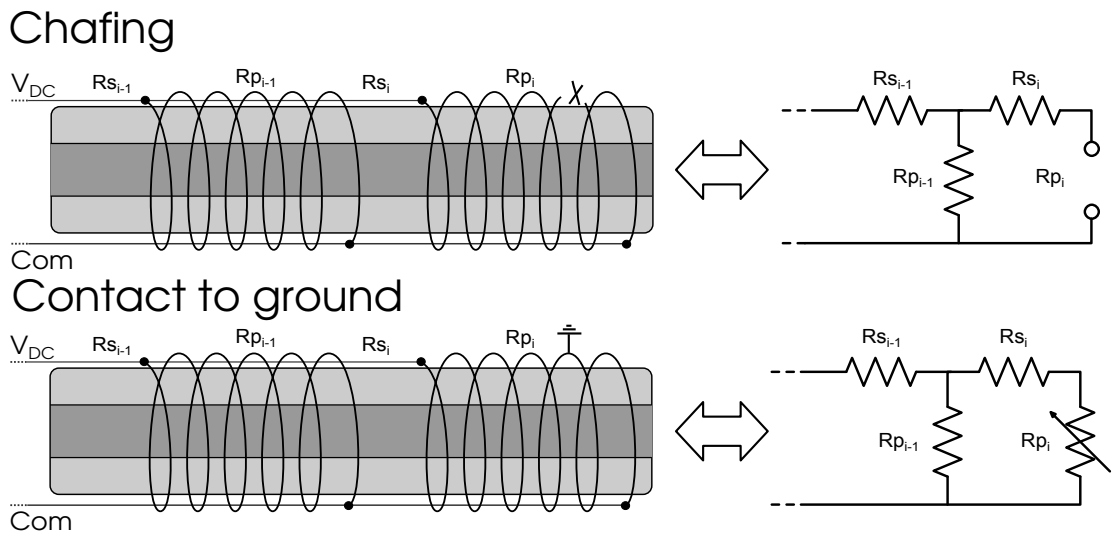

Figure 3.4: Equivalent circuits of possible faults happening on the i mesh using the protective mesh in parallel.

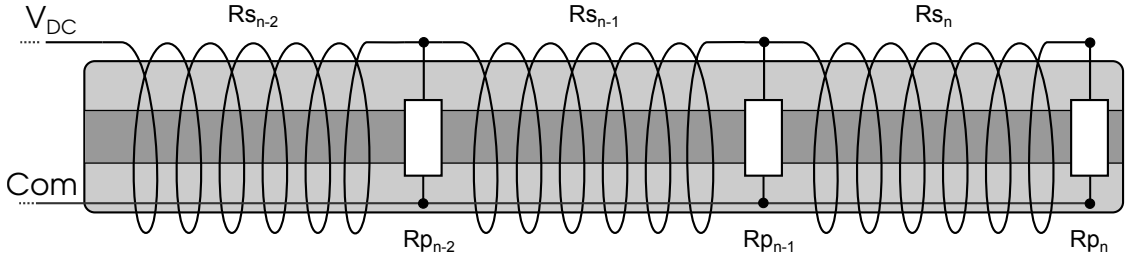

Figure 3.5: Diagram of sensor architecture using the protective mesh as the series element.

As in the parallel architecture, the equivalent circuit can be modified to represent certain types of faults, as shown in Figure 3.6. When a chafing fault occurs it can be modelled by replacing with an open circuit the series resistor of the affected mesh i disconnecting the rest of the network from that mesh onwards. A contact to the ground fault can be modelled with a short circuit between the series resistor i and the ground, and the values of that resistor can change depending of the fault location in the mesh. The variable resistor is proportional to the length of the winding from the leftmost solder joint to the spot where the fault happened. The value of this variable resistor can vary in the range of 0 to Rs_i.

3.2.2 Architecture performance comparison

Given a specific sensor architecture and equivalent circuits, for each type of fault that the sensor can detect, it is possible to compute the equivalent resistance of the network. An example of such computation is shown in Figure 3.7, applying a fault of each type in every mesh of the network one at a time. Results shown in Figure 3.7 assume a sensor with 10 meshes following a protective mesh in series architecture, $R_s = 100\ \Omega$

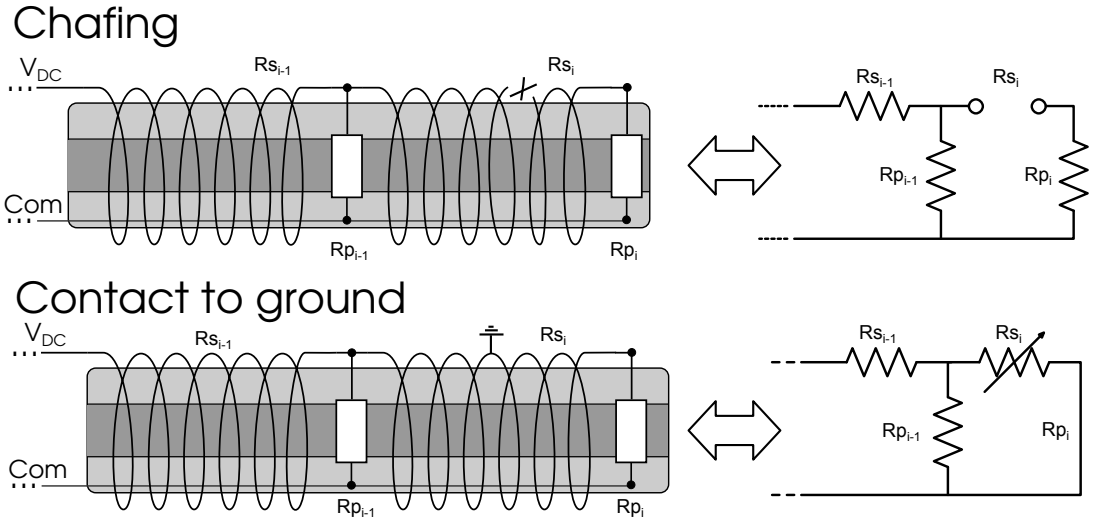

Figure 3.6: Equivalent circuits of possible faults happening on mesh i using the protective mesh in series.

and $R_p = 1\ M\Omega$. Each type of fault generates a specific equivalent resistance for the network. The equivalent resistance of a fault in the first mesh has been omitted because its value is infinite.

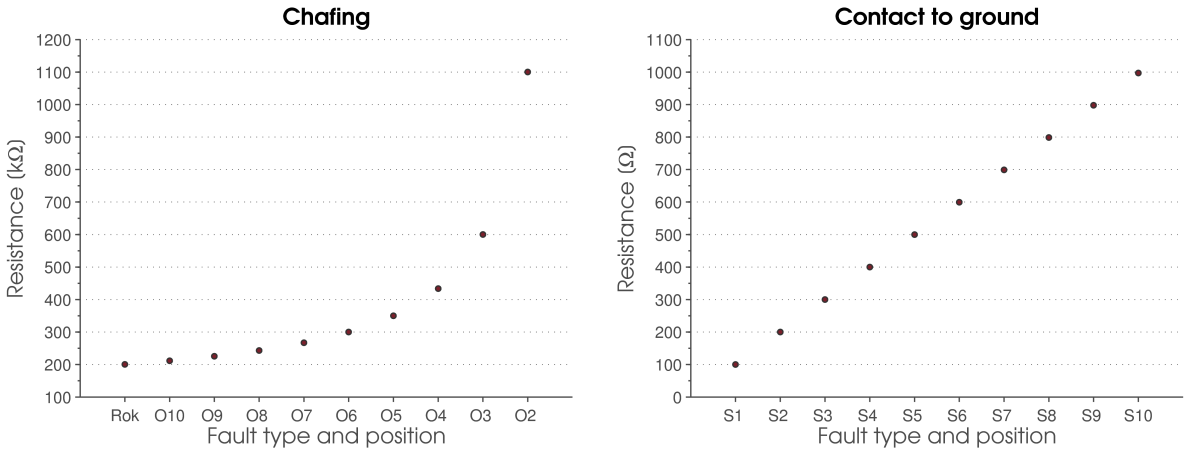

Figure 3.7: Results computed for each type of fault on a sensor with 10 meshes following a protective mesh in series architecture. (O for open- and S for short-circuit)

The performance of both architectures can be compared. The performance is given by the minimum relative difference between equivalent resistances of each fault after the results sorted

$$\min\left\{\frac{(R_i - R_{i-1})}{R_i}\right\}, \quad for \quad i = 2, 3, \ldots, n \tag{3.4}$$

where i is the index of the fault, R_i is the equivalent resistance of the network of index i and n is the number of possible equivalent resistance values for the network.

The relative difference between the equivalent resistance of each fault shows the minimum theoretical accuracy of a measurement to ascertain the location and type of

fault. This theoretical accuracy is expressed as a fraction of full scale of a multiscale measurement system, with one scale for each value of equivalent resistance that the sensor can have, depending on type and location of the fault. Therefore, in order to reduce the number of scales in the measurement system, the practical needed accuracy must be larger.

However, in addition to type of sensor architecture, other effects can change the performance of the sensor. The ratio of the parallel to series resistance elements of the network also plays a critical role in the performance of the sensor. In order to study the influence of the R_p/R_s ratio in the performance of the sensor, it was computed the performance for both types of architecture (Figure 3.8). A straightforward analysis shows that the protective mesh in series gives the best performance and that R_p should be larger than R_s by several orders of magnitude. As the number of meshes in the network increase so does the R_p/R_s ratio that gives the best performance. However, the practical implications of accurate measurement of very large resistance values limits the maximum number of meshes in a network.

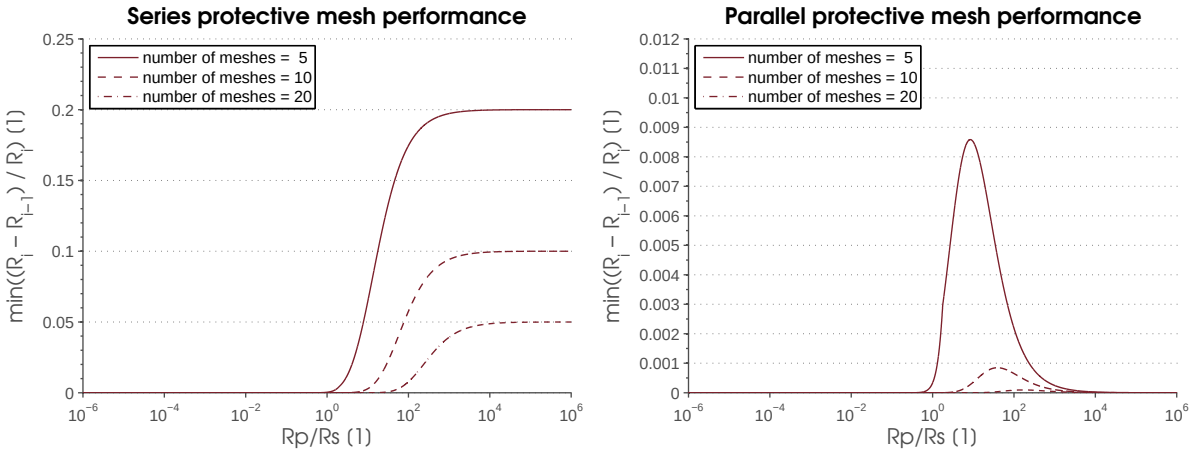

Figure 3.8: Performance of each architecture as a function of R_p/R_s ratio for different number of meshes in the network.

3.3 Effect of temperature

Each fault type and location is identified by comparing sensor resistance with a pre-computed resistance table. It is critical that external conditions do not change the resistance of the elements that form the network. One of the most important factors to consider is the resistance temperature coefficient of the materials used in the sensor. As described in the requirements, the sensor must withstand and operate at temperatures ranging from -50^oC to 100^oC. The sensor must also function correctly in an environment that has strong temperature gradients, with sections of the sensor subjected to different temperatures.

To implement the sensor, one of the materials that needs to be chosen to compose the protective mesh must be available in a form of a wire. Several factors had to be taken into account, including mechanical properties, electrical resistance and temperature coefficient as well as cost and availability.

Using the protective mesh in series, the ideal material to form the protective mesh presents a low value resistance with negligible temperature coefficient. From several materials that can be used, copper and manganin alloy were simulated to evaluate effect of temperature in sensor performance given their price and availability. Copper has one of the lowest resistivity with a ρ value of 1.69 $\mu\Omega.cm$ and it is highly available. However, its temperature coefficient is very high, reaching 4300 $ppm/^oC$ [23]. Manganin, on the other hand, has a higher electrical resistivity, 43 $\mu\Omega.cm$, but a much lower temperature coefficient, of only ± 10 $ppm/^oC$. However, since the variation of resistance with temperature of manganin is not monotonic, it is preferable to specify a narrow range of temperature where it can be linearised. For the temperature range under test, manganin shows a -0.4% resistance variation from room temperature to -50^oC and -0.1% from room temperature to 100^oC, respectively [24].

For the offset elements, precision thin film NiCr (Nickel-Chromium) based tertiary alloy resistors in a SMT (Surface Mount Technology) package were used. From the datasheet, the selected resistors have a ± 25 $ppm/^oC$ temperature coefficient. This range of temperature coefficient defines, according to international standards, the positive and negative allowed chord slopes of the resistors and do not define the behaviour of change in resistance as function of temperature [25].

As shown in Figure 3.9, when the sensor is subjected to a temperature variation while healthy or when suffering from a chafing fault, the material does not hinder the ability to detect defects in the mesh. Dots mark the equivalent resistance of the network at 20^oC and the error bar the variation in resistance for a temperature range of -50 ^oC to 100 ^oC. The considered network has a 1 m protective mesh made of a 0.15 mm diameter copper wire with a pitch of 10 mm wrapped around a main conductor with 10 mm diameter. Parallel resistors of 100 $k\Omega$ were used.

When detecting chafing faults, the variation in the resistance of the parallel element dominates the variation of the equivalent resistance of the sensor. Given the resistance values chosen for the simulation, the resistance values used in the simulation, a 1% variation in R_p of all meshes result in a 0.995% variation in equivalent resistance of the sensor, while the same variation applied to the R_s of all meshes results only in a 0.005% change in sensor resistance. As the parallel elements are NiCr resistors with low temperature coefficient, the variation in equivalent resistance of the sensor does not affect system operation.

However, when the sensor suffers from a contact-to-ground fault, a series element gets direct contact to ground, resulting in the series resistance dominating the equivalent resistance of the network. In this situation, a 1% variation in R_p resistance introduces

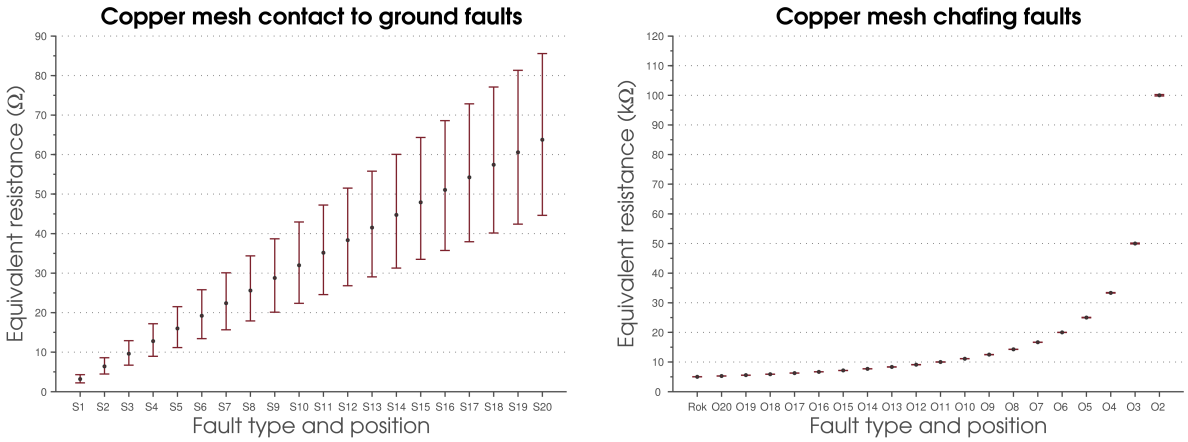

Figure 3.9: Equivalent resistance for each type of fault and location in the sensor with the protective mesh made of copper wire.

only a 0.004% change and the same variation in R_s results in a 0.995% change in the equivalent resistance of the sensor. Since the series resistor is made of a copper wire that has a high temperature coefficient, the ability to identify the location of the fault is compromised in the desired temperature range.

Using manganin wire as the series resistance (Figure 3.10) the same scenario occurs, however, as the temperature coefficient of manganin is very low, the resistance variation as a function of temperature is negligible for both types of faults. In Figure 3.10, the dots mark the equivalent resistance of the network at 20^oC. The considered network has a 1 m protective mesh made of a 0.15 mm diameter manganin wire with a pitch of 10 mm wrapped around a main conductor with 10 mm diameter. Parallel resistors of 100 $k\Omega$ were used.

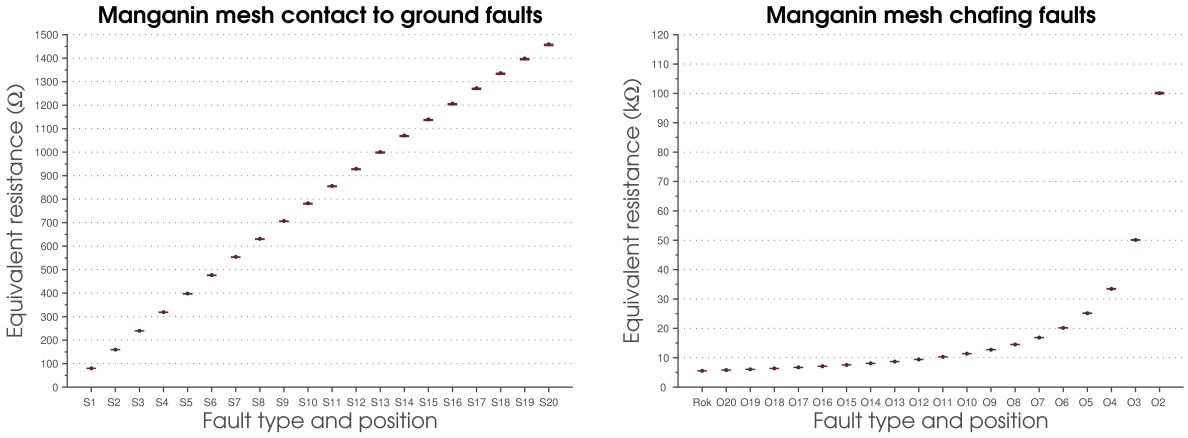

Figure 3.10: Equivalent resistance for each type of fault and location in the sensor with the protective mesh made of a manganin wire, in the temperature range from -50^oC to 100^oC.

3.4 Prototype

A prototype has been made by replicating a 20 m sensor with 1 m meshes and pitch of 1 cm. The mesh size and pitch were scaled down to fit the same resistance values into a sensor with 2 m length. The sensor is wrapped around an 8 mm diameter cable, including a PVC (Polyvinyl chloride) insulator and follows the protective mesh-in-series architecture, as described in Subsection 3.2.1. The protective mesh is made of 0.15 mm enamelled manganin wire and the parallel elements are 100 $k\Omega$ SMD (Surface Mount Device) NiCr resistors in an 0805 package. The return conductor is made of 0.15 mm enamelled copper wire. The SMD resistors are soldered between the protective mesh and the return conductor and held in place along the cable by an epoxy adhesive. The full assembly was then covered with a polyolefin heat shrink tubing to enhance physical, chemical, and electrical properties of the assembly. The sensor fully assembled is shown in Figure 3.11. The red and brown lead wires connect to the measurement system.

Figure 3.11: Prototype sensor.

Giving the specifications for the prototype sensor built, the scales for the measurement system can be calculated. Although the performance needed for the measurement system was computed considering that it had a scale for every possible value of equivalent resistance of the network, this strategy was not applied to the designed system in order to reduce its component count and therefore its size. From the $2 \times n$ scales used in the theoretical model, where n is the number of meshes in the network, the number of scales was reduced to the minimum, while keeping the accuracy for each scale above 1%. Keeping the accuracy above 1% simplifies measurement topology and components selection. Table 3.1 summarizes the scales used, as well as the resolution, test current, and required accuracy for each scale. The measurement system uses 4 main scales and a gain factor for each scale, increasing the number of scales to 8.

Table 3.1: Measurement system's scales.

Range	**Resolution**	**Test Current**	**Accuracy (required)**
1 $k\Omega$	244 $m\Omega$	1.25 mA	<5% Full Scale
2 $k\Omega$	488 $m\Omega$	1.25 mA	<2% Full Scale
5 $k\Omega$	1.22 Ω	250 μA	*NA*
10 $k\Omega$	2.44 Ω	250 μA	<2% Full Scale
50 $k\Omega$	12.21 Ω	25 μA	<1% Full Scale
100 $k\Omega$	24.42 Ω	25 μA	<15% Full Scale
500 $k\Omega$	122.1 Ω	2.5 μA	<10% Full Scale
1 $M\Omega$	244.2 Ω	2.5 μA	*NA*

Chapter 4

Measurement system design

In this chapter is presented the measurement system architecture and the operation of corresponding subsystems are described. It is also performed a worst case scenario analysis of the measurement system accuracy.

4.1 Requirements

In addition to the accuracy requirements for resistance measurement imposed by the sensor construction, several requirements were defined for the measurement system:

- Periodical measurements of the sensor resistance.
- Ability to sleep between readings.
- Wireless communication.
- Low power.
- Low cost.

4.2 Arquitecture

The measurement system is composed of 3 subsystems: the processor, the source and measurement subsystem and the display subsystem, as shown in Figure 4.1. Each of these subsystems are in a different printed circuit board (PCB) for modularity.

Each PCB connects to each other by two miniature headers that provide access to both signals and power through the system.

As the system is composed of different modules, it easier to test each subsystem separately and, if needed, connect and test new subsystems.

4.2.1 Processor subsystem

The processor board was already designed prior to start of the project. The central component of this subsystem is a JN5140-001-Myy wireless microcontroller module. This

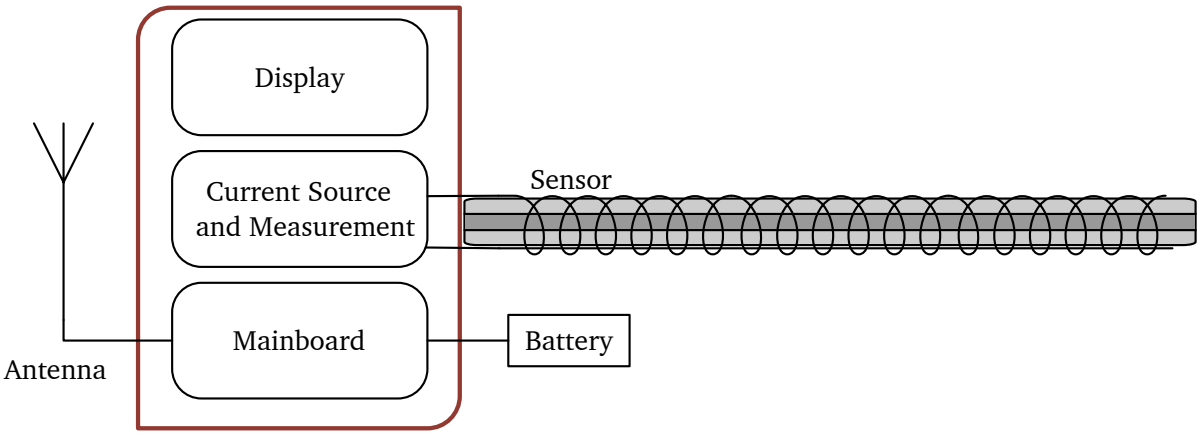

Figure 4.1: Diagram of the measurement unit and its interfaces.

module has a JN5148 IC, a crystal oscillator, 512kB of flash memory and a matching network with an internal antenna (M00 option) or an external antenna (M03 option). In addition, if the high power option is selected, an external Power Amplifier (PA) and Low Noise Amplifier (LNA) come equipped in the module for increased transmitting power.

The JN5148 IC, whose block diagram is shown in Figure 4.2, is a low power microcontroller featuring a 32 bit RISC processor with up to 32 MHz clock speed, 128 kB of ROM and RAM and a 2.4 GHz IEEE 802.15.4 compliant wireless transceiver. Given the large memory size, the processor can run a network stack together with an application allowing it to run as the main processor in certain end uses, as well as a co-processor enabling wireless capabilities with zero overhead to a main processor. The JN5148 is compatible with several wireless network protocols including ZigBee Pro. Both module and integrated circuit were developed by the fabless semiconductor company Jennic, now acquired by NXP Semiconductors and operating as NXP Low Power RF.

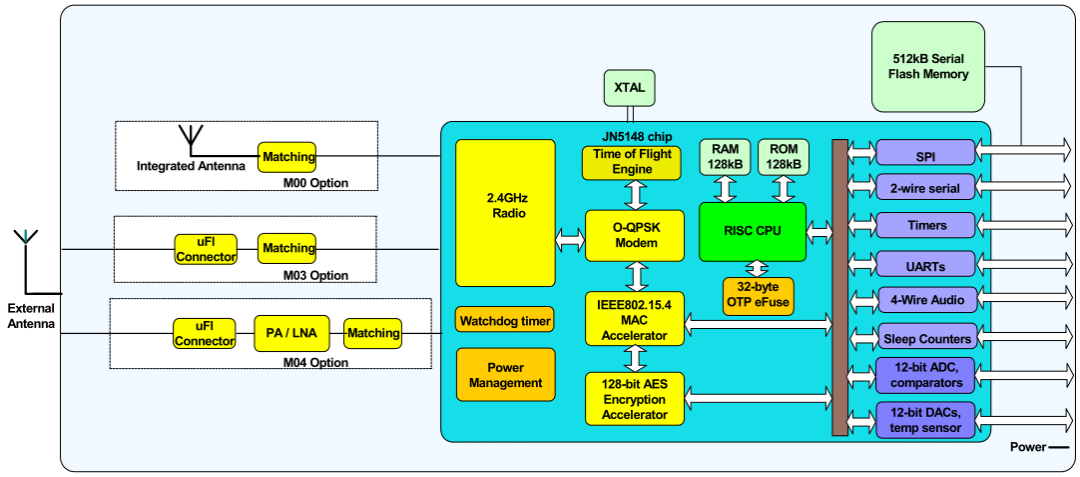

Figure 4.2: JN5140-001-Myy wireless microcontroller module block diagram.

The processor board, shown in Figure 4.3, has all the necessary requirements to enable programming the module flash memory with firmware via serial interface.

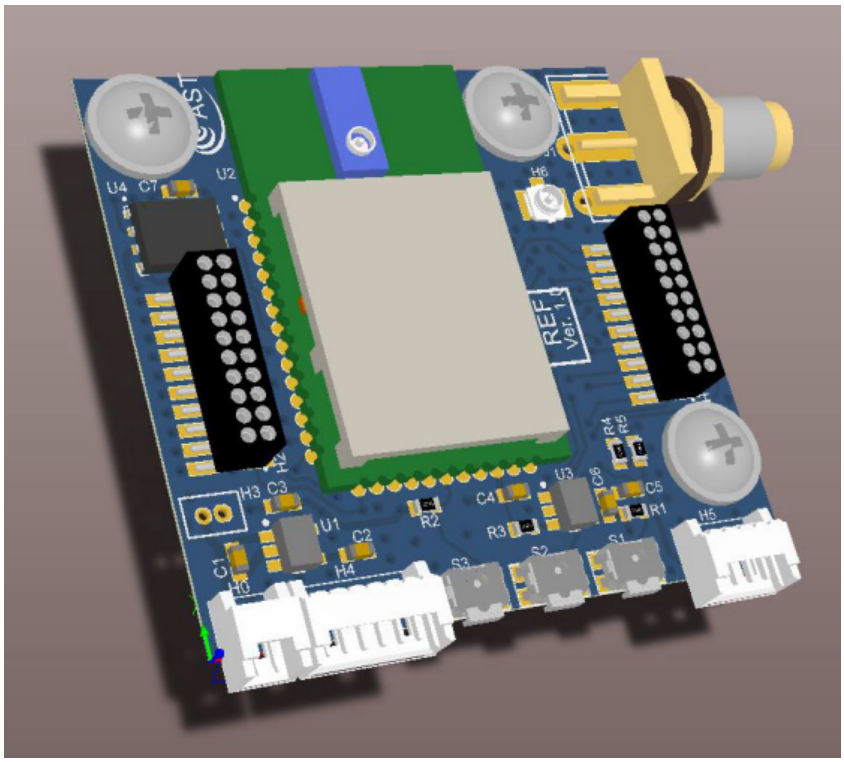

Figure 4.3: 3D rendering of the processor board.

4.2.2 Current source and measurement subsystem

The current source and measurement board is divided in three fundamental sections for the resistance measurement of the sensor: a current source, an analogue conditioning circuit and a analog to digital converter. Each of these three sections are contained into the same PCB, shown in Figure 4.4.

A) Current source

The current source circuit uses a two operational amplifier configuration as shown in Figure 4.5. The operational amplifier U1 sets a voltage drop across R1 equal to V_{ref}. This voltage will force a current through R1 equal to $\frac{V_{ref}}{R1}$. As no current follows in or out the gate terminal of Q1, the same current flows through R2. The voltage drop in R2 is set by U2 through RSx sourcing a current equal to $\frac{V_{R2}}{RSx}$ to the load. The maximum voltage that this configuration can apply to the load while maintaining the defined current and assuming $Rds_{Sx} = 0$, can be expressed as:

$$V_{compliance} = V_{DD} - RSxI_{RSx} - Rds_{ON}(I_{RSx}, V_{GS})I_{RSx} \tag{4.1}$$

,where V_{DD} is the suplly voltage, I_{RSx} is the current thought the reference resistor RSx, Rds_{ON} the resistance between the drain and source of the Q2, that is a function of the current flowing thought it, in this case I_{RSx}, and the voltage applied between the gate and source V_{GS}.

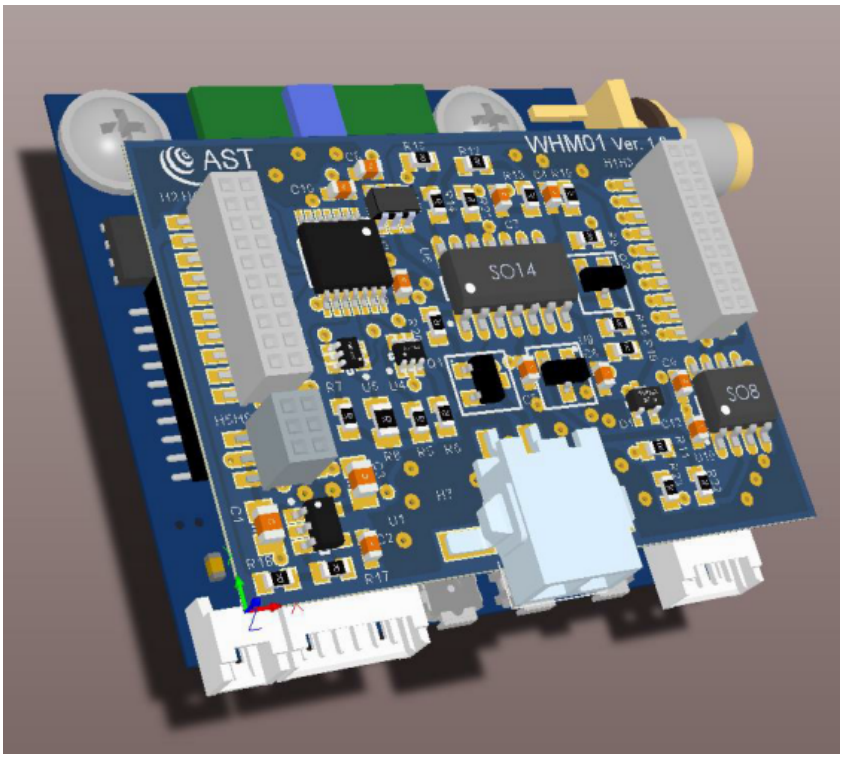

Figure 4.4: 3D rendering of the current source and measurement board.

This configuration has the advantage of sourcing current with only one single voltage supply and using a voltage reference to ground. Thus, this voltage reference can be used for the whole measurement circuit, removing the need for knowing the exact value of the reference voltage, as long as this value stays stable.

Other configurations for current sourcing are shown in Figure 4.6. These configurations present reduced components count, but each configuration presents disadvantages for this specific application. In the circuit shown in Figure 4.6(a), the set current is equal to $\frac{V_{DD}-V_{ref}}{Rscale}$. Given that the supply voltage is not as stable and accurate as a voltage reference, this severely hinders the current source performance.

In Figure 4.6(b) the voltage reference is a shunt reference whose reference voltage is set regarding the supply rail and thus the set current is equal to $\frac{V_{ref}}{Rscale}$. However, in this configuration the voltage reference cannot be used in the whole signal chain when using an ADC that has a voltage reference related to ground. Also, shunt regulators normally have larger quiescent currents than series voltage references.

In Figure 4.6(c) the set current is equal to $\frac{V_{ref}}{Rscale}$. However, the circuit works as a sink rather than a current source. This prevents the measurement of the voltage in the load with a single-ended conditioning chain. Thus, introduction of a new component in the signal chain front-end to measure the differential voltage across the load is needed. The component could be both an operational amplifier in a difference configuration or an instrumentation amplifier.

In Figure 4.6(d) the set current is equal to $\frac{V_{ref}}{Rscale}$. This configuration saves one

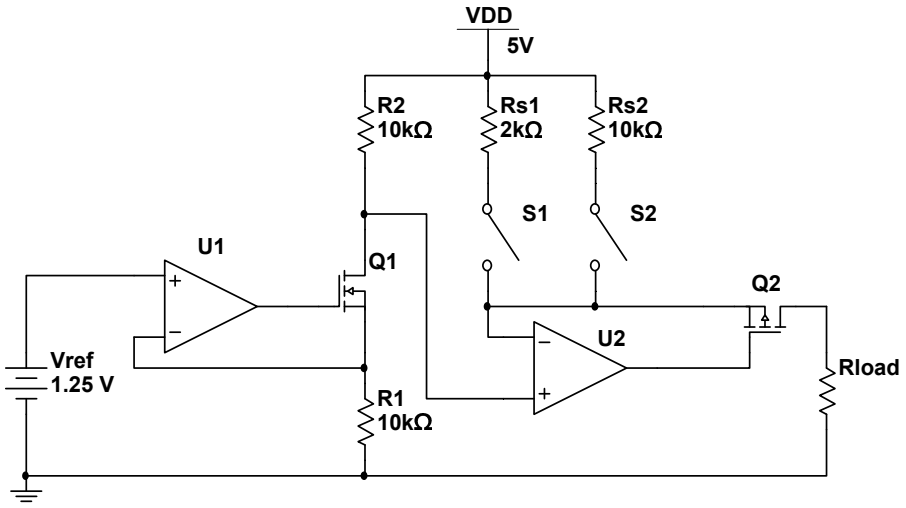

Figure 4.5: Current source implemented

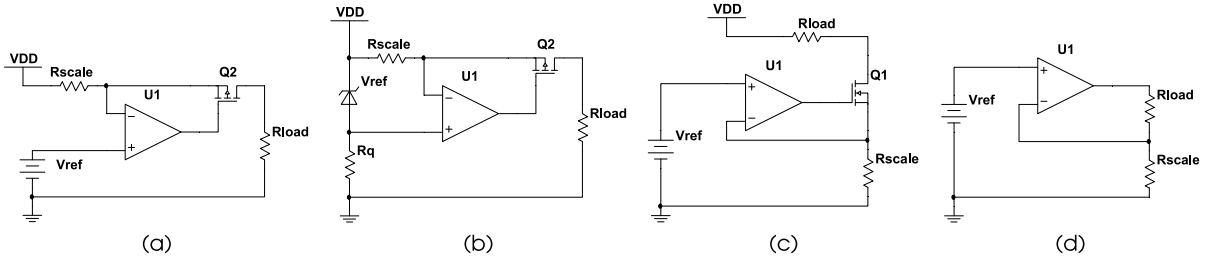

Figure 4.6: Schematics of several topologies of single supply current sources and sinks.

transistor, although the voltage supplied to the load must be the same as the operational amplifier supply voltage. Additionally, the current sources rely on the linearity of the operational amplifier. This could bring trouble specially when the amplifier is operating near its rails.

B) Analogue conditioning

The analogue conditioning circuit is compose of an amplifier, followed by a two pole low-pass filter. The amplifier is implemented using an operational amplifier in a non-inverting configuration. Feedback to the amplifier can come directly from the output or from a voltage divider. This selection is made by a single pole double throw CMOS switch that enables switching between gain = 1 and gain = $\frac{R3}{R4} + 1$. For this application the gain is either 1 or 2. The two pole low-pass filter is obtained using the Sallen-Key low-pass configuration as shown in Figure 4.7.

The transfer function of this configuration can be expressed as

$$H(s) \quad = \quad \frac{{w_0}^2}{s^2 + 2\alpha s + {w_0}^2} \tag{4.2}$$

where

$$w_0 = 2\pi f_0 = \frac{1}{\sqrt{R_1 R_2 C_1 C_2}} \tag{4.3}$$

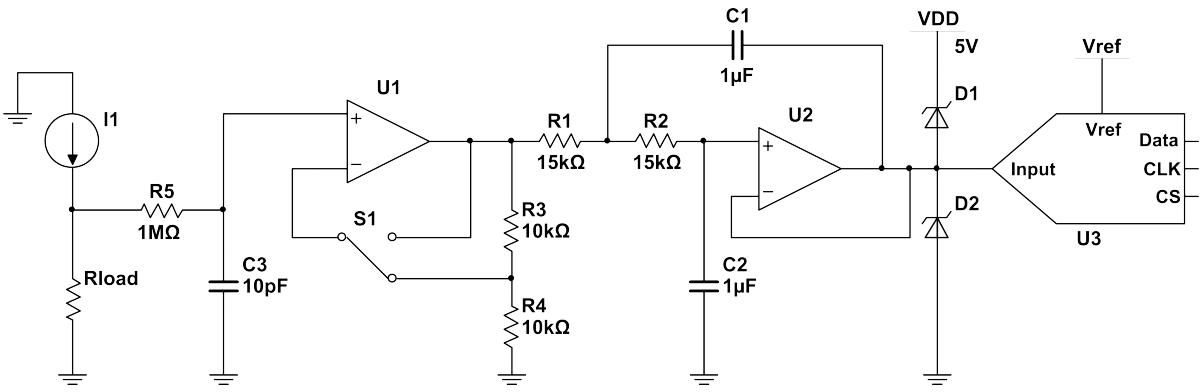

Figure 4.7: Signal conditioning schematic.

and

$$\alpha = \frac{1}{2C_1}\left(\frac{R_1 + R_2}{R_1 + R_2}\right) \tag{4.4}$$

Given the nature of the equation, it is easier to use an available filter simulator to graphically evaluate the performance of the filter. A 10 Hz filter with a damping ratio $\zeta = 1$ was selected. This means the system is critically damped and thus does not overshoot or undershoot in fast transitions. Since this configuration is an active filter, the output impedance is low, hence the input of the ADC can be directly connected to the output of the filter.

C) Analogue to digital conversion

In order to perform the analogue to digital conversion a Successive-Approximation Register (SAR) ADC is used. A SAR ADC, as shown in Figure 4.8, uses a digital-to-analogue converter and a high speed comparator to perform the conversion, using a binary search algorithm.

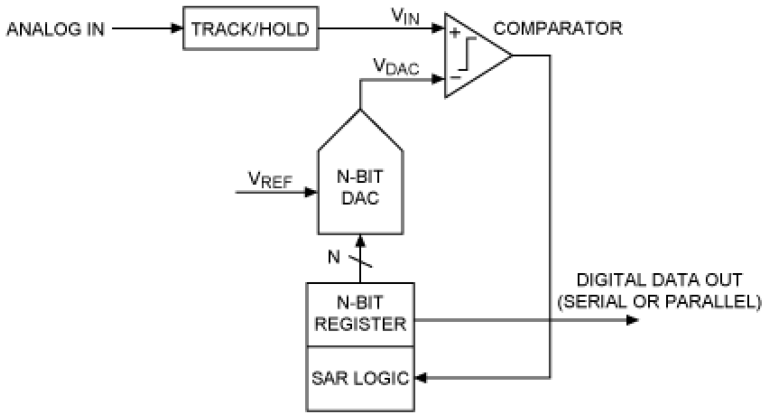

Figure 4.8: Simplified N-bit SAR ADC architecture [8].

To perform the conversion the input is sampled and held during the conversion cycle. Following that, the most significant bit of the register is set and the DAC outputs $\frac{V_{ref}}{2}$.

This value is compared to the voltage in the holder. If the input voltage is higher than the output the most significant bit of the register remains set, otherwise it resets to zero. Subsequently that, the next most significant bit is set high forcing a new value to the DAC output and another comparison is performed. This process repeats for every n bit of the ADC. Therefore, every conversion cycle has n comparisons where each of reduces the error to a theoretical minimum of one least significant bit between the input voltage and the DAC output.

A SAR type ADC is used to demonstrate the system feasibility. It utilizes a low cost ADC that could meet the accuracy requirements defined in Section 3. A 12-bit SPI ADC (MCP3201) from Microchip was selected. The voltage reference pin of the ADC is tied to the voltage reference IC making the accuracy of the reference not needed for the measurement of the sensor resistance.

4.2.3 Display subsystem

A display board was made for prototype and prove of concept, as the system does not need human interface besides for commissioning. The display board central component is a Nokia 6100 LCD display. Supporting the display the board contains all necessary parts including a voltage regulator and boost converter for the LCD back light. Disabling the voltage regulator enables and disables the LCD or back light respectively. The display board PCB is shown in Figure 4.9.

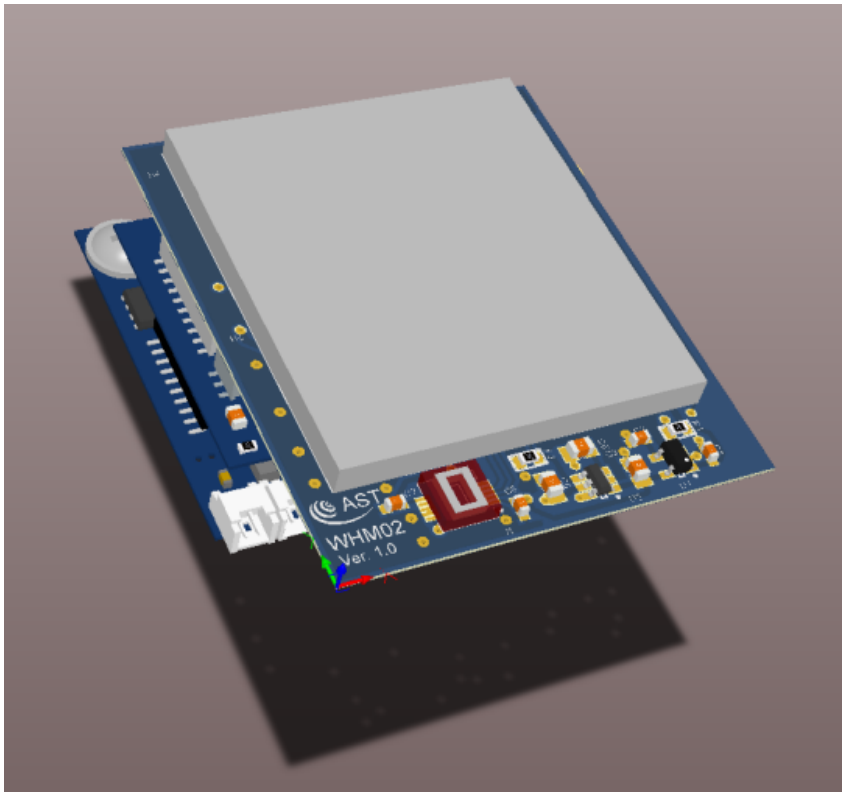

Figure 4.9: 3D rendering of the display board.

4.3 Error budget

An error budget of the full measurement system is shown in Table 4.1 and Table 4.2 and is performed according to the method described in [26], using a worst case scenario approach. The budget is divided in two circuits: the current source and the analogue condition and digital conversion circuits, analysed in Table 4.1 and Table 4.2, respectively. The various sources of error are normalize to full scale and expressed in ppm

The sum of all error sources is called the total unadjusted error and is shown in Table 4.3. However, some error sources can be cancelled through calibration. Those that cannot be calibrated are shown in colour and their sum represents the resolution error of the measurement system. The effect on error of temperature variation separately in each table.

4.3.1 Current source error budget

The resistors used have a 0.1 % tolerance and a temperature coefficient of 25 ppm/°C. This results in a 1000 ppm error per resistor. Also, assuming a 75°C temperature variation this adds 1875 ppm of error. The noise generated by the resistors is ignored as their contributuion to the error budget is very low.

The initial value of the voltage reference, as well as its temperature drift and ageing, does not affect the measurement of the sensor resistance, as the measurement is ratiometric. However, the voltage output noise generated by the voltage reference at low frequencies (higher frequencies are filtered out by the low-pass filters and software averaging) must be taken into account. From the device datasheet [27], the voltage output noise is 33 μVpp. As the noise generated follows a Gaussian distribution the value can be converted to rms using the industry standard peak-to-peak to rms (crest factor) of 3.3. This results in 5 $\mu Vrms$, representing a 2 ppm error.

Both U1 and U2 are operational amplifiers [28] in unity gain configurations, thus their error sources are amplified by a gain of 1. The voltage and current noise generated by U1 and U2 is ignored since their contribution to the error budget represents less than 1 ppm. In U1 the input bias currents only generates error by the inverting terminal, as the non-inverting terminal is connected directly to the voltage reference. The inverting terminal sources or sinks a bias current that increases or decreases the current flowing through R1 and R2.

For the operational amplifier U2 the input bias current of the non-inverting terminal generates the same error that the input bias current of U1. However, in U2 the inverting terminal generates a different error for each scale resistor used. The higher the scale resistor used the larger the input bias error generated.

Furthermore, the effect of the resistance of the switches, in form of N-channel FET transistors that select between scales, were evaluated. From the datasheet [29], at the operating V_{GS} and current the on resistance is approximately 520 $m\Omega$. This resistance

adds to the set scale resistor. The smaller the scale resistor the more impact it will have in the error of the scale current.

For the total error it is considered the worst case scenario between the effect of the input bias currents of U2 and the effect of S_x Rdson.

4.3.2 Analogue conditioning and digital conversion error budget

The gain resistors of the amplifier also contributes to the measurement system error. The other resistors of the analog circuit do not contribute to error, as their value does not need to be precise to ensure the system proper operation.

The operational amplifier U1 [28] has a selectable gain operated by S1 (a single pole double throw analog switch). This gain is selectable between $gain = 1$ and $gain = 2$. Therefore, to consider the worst case scenario, the error sources from U1 must be multiplied by a factor of 2. The error generated by the input bias current of U1 comes from the voltage developed by U1 bias current across R5.

The operational amplifier U2 follows a Sallen-Key low-pass filter configuration with unity gain. The error from the input bias current of the amplifier comes from the voltage developed by the U2 input bias current of the non-inverting terminal across both R1 and R2.

Several parameters are used to evaluate the performance of the ADC [30]. The offset error quantifies offset from the device transfer function to the ideal transfer function. The gain error is a deviation from the ideal slope of the transfer function. Both the offset error and the gain error can be removed with calibration. The INL (Integral Non-Linearity) describes departure from an ideal linear transfer curve for an ADC. It does not include the offset error and the gain error. This value is a fundamental figure of merit when selecting an ADC and cannot be removed with calibration.

4.3.3 Total error

The sum of errors generated by the current source and the analog conditioning circuit are shown in Table 4.3. As noted, without any calibration the measurement system satisfies the defined requirements if the effect of temperature is not taken into account. If the system is calibrated, even with the considered ΔT, it satisfies the defined requirements. Moreover, a temperature compensation scheme could be applied to minimize the effect of temperature in the accuracy of the instrument.

Table 4.1: Worst case scenario error budget of the current source circuit. The errors from sources that cannot be removed by calibration in room temperature are shown in colour.

Error source		Error
Resistors		
R1	0.1 % precision resistor	1000 ppm
R1 with $\Delta T = 75\ ^oC$	$25\ ppm \times \Delta T$	1875 ppm
R2	0.1 % precision resistor	1000 ppm
R2 with $\Delta T = 75\ ^oC$	$25\ ppm \times \Delta T$	1875 ppm
Rsx	0.1 % precision resistor	1000 ppm
Rsx with $\Delta T = 75\ ^oC$	$25\ ppm \times \Delta T$	1875 ppm
Vref		
0.1 Hz to 10 Hz Noise	$5\ \mu Vrms/2.5\ V$	2 ppm
U1		
Offset Voltage	$50\ \mu V/2.5\ V$	20 ppm
Offset Voltage drift $\Delta T = 75\ ^oC$	$18.8\ \mu V/2.5V$	15 ppm
Avol gain error	$1/100\ dB \times 2.5\ V$	9.6 ppm
Input bias current	$300\ pA/250\ \mu A$	1.2 ppm
U2		
Offset Voltage	$50\ \mu V/2.5\ V$	20 ppm
Offset Voltage drift $\Delta T = 75\ ^oC$	$18.8\ \mu V/2.5V$	15 ppm
Avol gain error	$1/100\ dB \times 2.5\ V$	9.6 ppm
Input bias currents		
when $Rscale = 2k\Omega$	$300\ pA/1.25\ mA + 300\ pA/250\ \mu A$	1.44 ppm
when $Rscale = 1M\Omega$	$300\ pA/2.5\ \mu A + 300\ pA/250\ \mu A$	121.2 ppm
Effect of S_x Rdson		
when $Rscale = 2k\Omega$	$520\ m\Omega/2\ k\Omega$	260 ppm
when $Rscale = 1M\Omega$	$520\ m\Omega/1\ M\Omega$	0.52 ppm
		TOTAL
Total Unadjusted Error without ΔT		3324 ppm
Total Unadjusted Error with ΔT		8980 ppm
Resolution error without ΔT		2 ppm
Resolution error with ΔT		5657 ppm

Table 4.2: Worst case scenario error budget of the analog condition and digital conversion. The errors from sources that cannot be removed by calibration in room temperature are shown in colour.

Error source		Error
Resistors		
R3	0.1 % resistor	1000 ppm
R3 with $\Delta T = 75\ ^oC$	25 $ppm \times \Delta T$	1875 ppm
R4	0.1 % resistor	1000 ppm
R4 with $\Delta T = 75\ ^oC$	25 $ppm \times \Delta T$	1875 ppm
U1		
Offset Voltage	(50 $\mu V \times 2$)/2.5 V	80 ppm
Offset Voltage drift $\Delta T = 75\ ^oC$	(18.8 $\mu V \times 2$)/2.5V	30 ppm
Avol gain error	(1/100 $dB \times 2$)/2.5 V	4.8 ppm
Input bias current	(300 $pA \times 1\ M\Omega \times 2$)/2.5 V	960 ppm
U2		
Offset Voltage	50 μ/2.5 V	40 ppm
Offset Voltage drift $\Delta T = 75\ ^oC$	18.8 μV/2.5V	2.4 ppm
Avol gain error	1/100 dB/2.5 V	15 ppm
Input bias current	(300 $pA \times 30\ k\Omega$)/2.5 V	7.2ppm
ADC		
INL	$\pm 1\ LSB$	244.1 ppm
Offset Error	$\pm 3\ LSB$	732.4 ppm
Gain Error	$\pm 5\ LSB$	1220.7 ppm
Gain Error drift $\Delta T = 75\ ^oC$	$\pm 0.1\ LSB$	24.4 ppm
		TOTAL
Total Unadjusted Error without ΔT		5304 ppm
Total Unadjusted Error with ΔT		9111 ppm
Resolution Error without ΔT		244 ppm
Resolution Error with ΔT		4051 ppm

Table 4.3: Total error of the measurement system.

Type	TOTAL
Total Unadjusted Error without ΔT	8628 ppm
Total Unadjusted Error with ΔT	18091 ppm
Total Resolution Error without ΔT	246 ppm
Total Resolution Error with ΔT	9708 ppm

4.4 Developed software

To demonstrate sensor communication capabilities, namely the ability to communicating from inside a vehicle or a building to a coordinator unit that manages wiring health status, a wireless processor was selected as the central processing unit. As stated in section 4.2, a JN5148 wireless microprocessor was selected. This processor has the capability of running several wireless firmware stacks.

In this work, the ZigBee Pro stack provided by NXP was used. Although it is a full feature ZigBee protocol, only two types of devices were used, the ZigBee coordinator and ZigBee End-Device [9]. The coordinator is responsible to initiate and maintain the network, as well as to manage the communication between the end-device and a computer. The end-device is the custom designed electronics module that measures the resistance of the wiring sensor and sends this information to the coordinator device. The general flow of the wireless communication is shown in Figure 4.10.

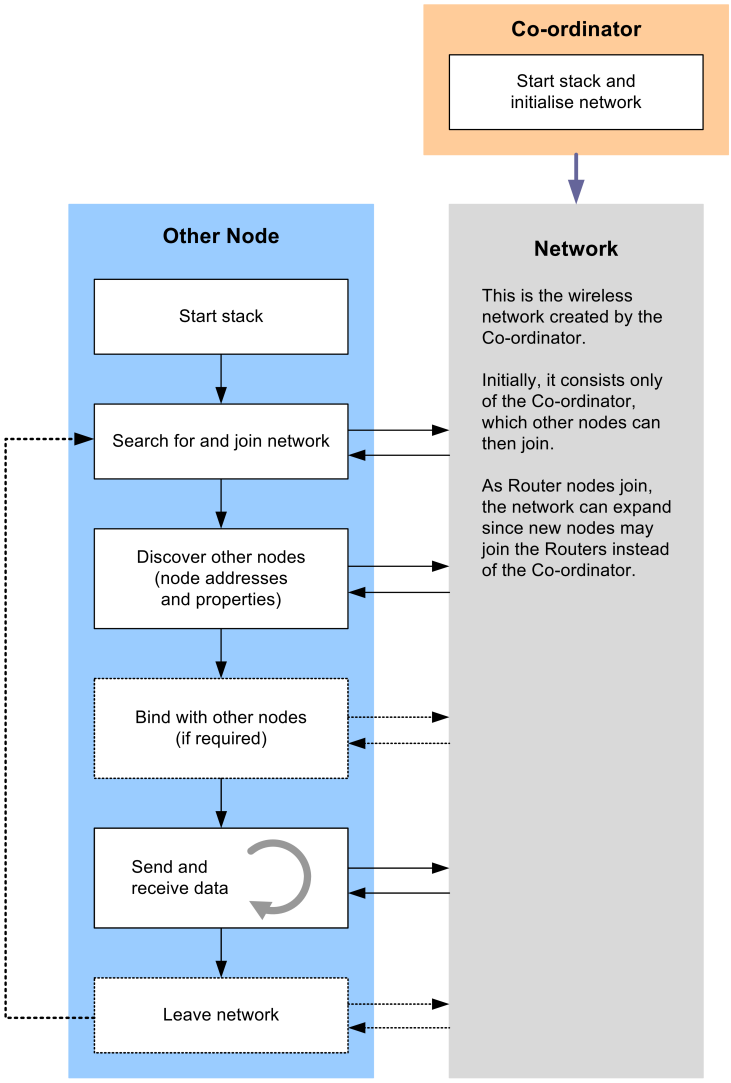

Figure 4.10: Wireless network life-cycle [9].

The end-device must measure the wiring sensor periodically and send the value of its resistance to the coordinator. It also updates the display unit for debug. However, the microprocessor runs an RTOS, called JenOS, the essential part of the software that reads the wiring sensor, is mostly sequential. The RTOS handles the run time of the user application and the ZigBee Pro Stack. The general flow of the developed software is display in Figure 4.11.

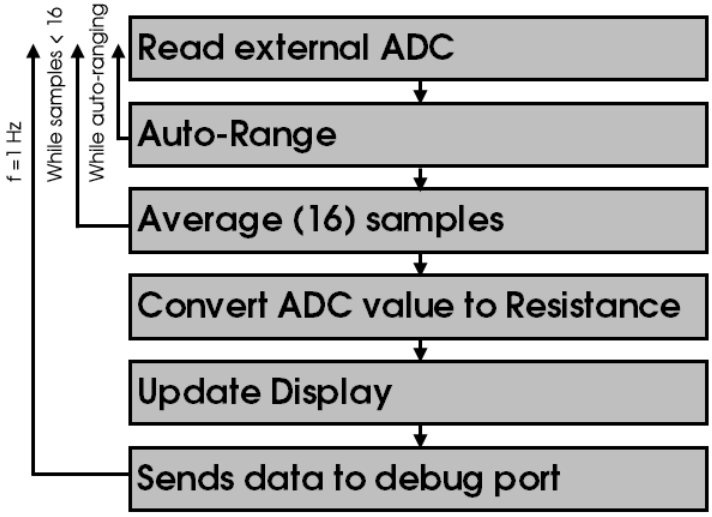

Figure 4.11: Flowchart of the measurement routine.

The **Read external ADC** is a function that reads data from the MCP3201 ADC present in the current source and measurement subsystem via a SPI bus.

The **Auto-Range** function guarantees that the best scale and gain factor is selected to read the resistance of the wiring sensor.

The function **Convert ADC value to Resistance** converts the value of the average samples to the corresponding value of resistance depending on the range and gain factor that was selected during measurement of those samples.

Chapter 5

Testing

This chapter presents the specified test plan and results for the most critical test procedures. These tests are related to interference from temperature variations in the surrounding environment. Also, the tests executed on the designed measurement unit are presented.

5.1 Sensor testing

Prior to testing, a detailed test plan was specified. A list of possible interferences that could affect the accuracy and performance of the measurement system was analysed. Furthermore, the possible interference from the sensor measurement to the main conductor was taken into account. For each of those interferences a requirement was specified. The full test plan is show in Appendix A.

- REQ001 – The sensor and measure cannot interfere with the normal behaviour of internal wiring.
- REQ002 – The power profile in the internal wiring cannot generate interference that makes it impossible to utilize the sensor or introduces errors outside defined tolerances
- REQ003 – Interferences from the external environment cannot interfere with the sensor measurement or with the normal behaviour of the internal wiring.
  - REQ004 – Variations in temperature cannot interfere with the measure of the sensor.
  - REQ005 – The existence of electromagnetic interference in the environment cannot interfere with the measure of the sensor.

For each of these requirements one or more test cases were specified. Each test has a detailed procedure to for its implementation. Some test give only qualitative results while others can give quantitative results. Also, the test plan is not static. As some tests were being conducted, new tests were included and the procedure updated in order to

reflect improved test conditions. The interface requirements and test cases were modelled in SysML.

5.1.1 General temperature drop

In order to study the effect of temperature below room temperature, namely sub-zero temperature, the prototype sensor was immersed in isopropyl alcohol due to its low temperature melting point. Gradually, carbon dioxide in solid form (dry ice) was added to the mixture, reducing its temperature. In Figure 5.1 is shown the experimental apparatus During the experiment, the resistance of the sensor and the temperature of the mixture were recorded. The resistance of the sensor as function of temperature is shown in Figure 5.2. From modelling, it is expected that the resistance of the sensor should lie between 5476 Ω and 5495 Ω for the tested temperature range. Furthermore, the resistance threshold that would deliver a useless measure from the sensor would be 5717 Ω; the expected temperature range would keep resistance values within acceptable limits.

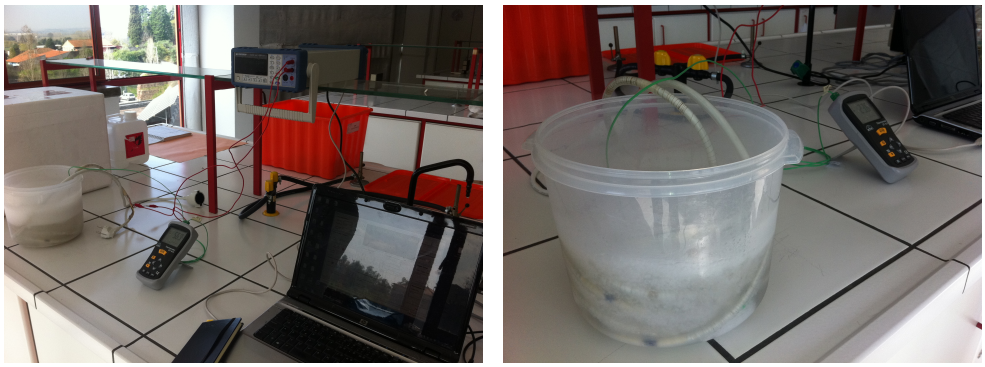

Figure 5.1: General temperature drop test setup.

5.1.2 General temperature rise

To test the sensor above room temperature, a new test setup was devised. The sensor was immersed in a metallic vessel filled with oil and the temperature slowly increased from room temperature up to 100^oC, as shown in Figure 5.3. As in the previous test, both temperature of the liquid and the resistance of the sensor were monitored during the test. The resistance of the sensor as a function of temperature is shown in Figure 5.4. It can be seen that high temperatures greatly impact the performance of the sensor. Latter, this was traced to the glue used to fix the SMD resistors to the cable and a new glue should be selected to maintain good electrical insulation at high temperature.

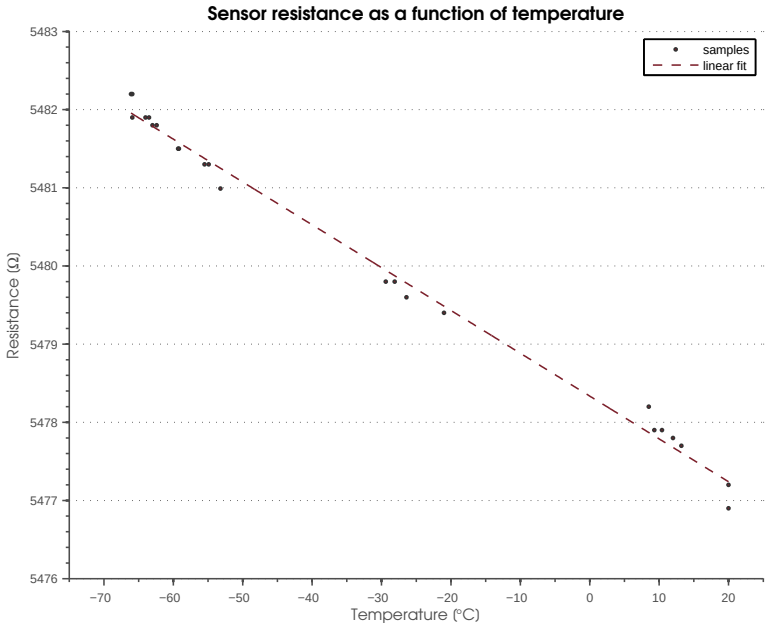

Figure 5.2: Resistance of the sensor as a function of temperature, from room temperature down to $-70\ ^{o}C$. Linear fit equation: $R(T) = -0.055T + 5478$.

5.1.3 Electromagnetic compatibility testing

Several tests were performed to assess electromagnetic interference, namely the impact on sensor sensitivity. However, since testing conditions were not ideal, these tests did not produce relevant quantitative data. To further refine the testing procedure regarding Electromagnetic Compatibility (EMC), emission and susceptibility tests inside an anechoic chamber should be performed according to RTCA/DO-160 test standard (Environmental Conditions and Test Procedures for Airborne Equipment). These tests would enable design improvement to validate the most demanding requirements for electronics equipment operation on board aircraft.

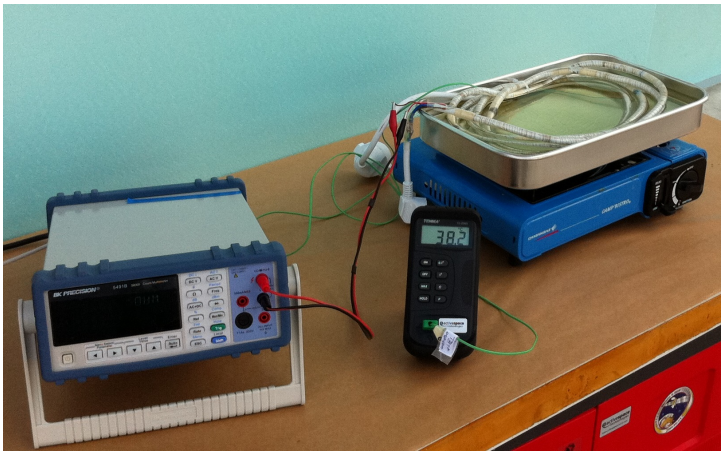

Figure 5.3: General temperature rise test setup.

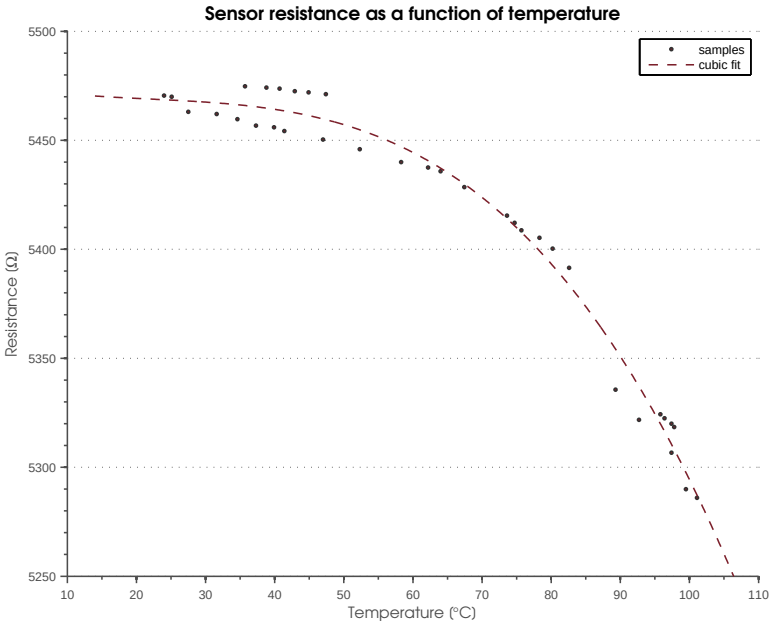

Figure 5.4: Resistance of the sensor as a function of temperature, from room temperature to 100 ^{o}C. Cubic fit equation: $R(T) = -3.4 \times 10^{-4}T^3 + 2.3 \times 10^{-2}T^2 - 6.6 \times 10^{-1}T + 5476$

5.2 Hardware testing

The measurement system defined in section 4 was tested to verify its accuracy for the envisioned measurement range from 100 Ω to 750 $k\Omega$. Nine through hole resistors with 0.1% tolerance were used to check the accuracy of the measurement system. Each test resistor was measured by the system for each scale and gain factor. The average of 20 consecutive measurements were used to calculate the measure resistance as shown

$$R = \frac{\frac{avg(digitized\ value)}{2^n - 1} R_{scale}}{gain factor} \tag{5.1}$$

, where n is the number of bits of the digitization.

Figure 5.5 shows the error range in the measurements choosing the scale with best accuracy for each test resistor. It must be noted that these values assume that the system was not calibrated.

Figure 5.6 shows several measurements using the 2 $k\Omega$ and 1 $M\Omega$ scales. Those measurements were done on through hole resistors with 0.1% tolerance. It can be seen that the measurement system is approximately linear. This allows for the system to be calibrated using only an offset and gain parameters. This, however, cannot be used to cancel the error induced by noise, gain, or offset due to temperature variations.

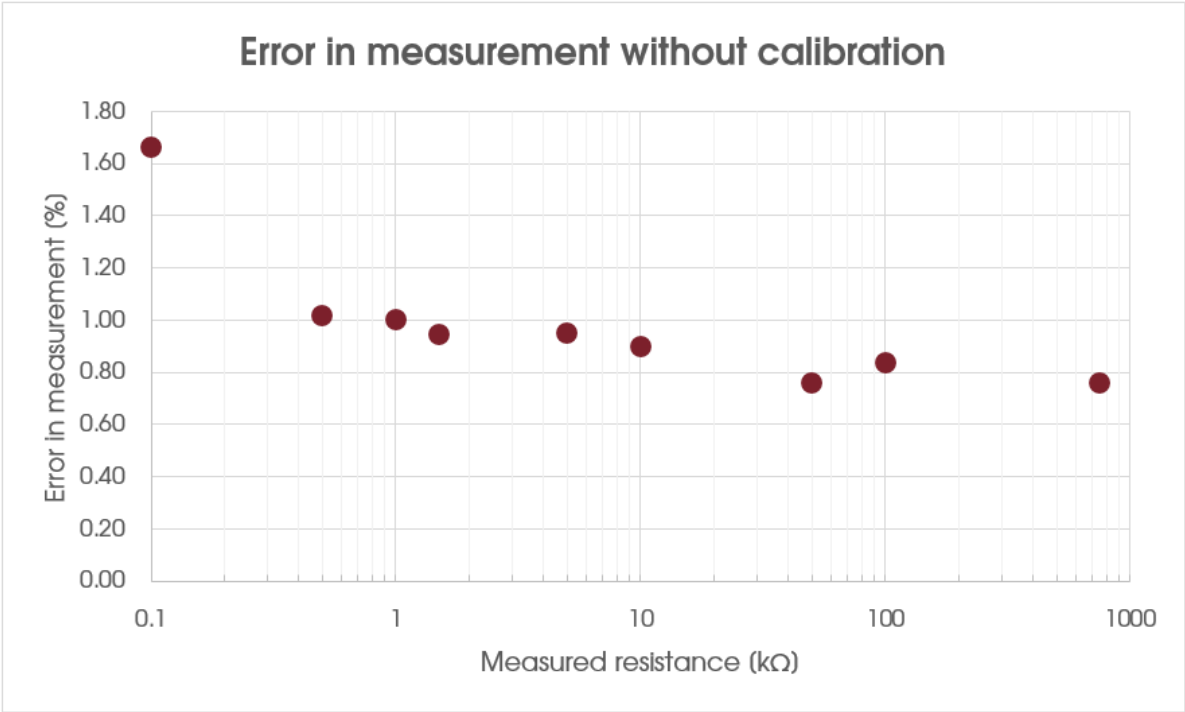

Figure 5.5: Measurement error for different chosen resistors.

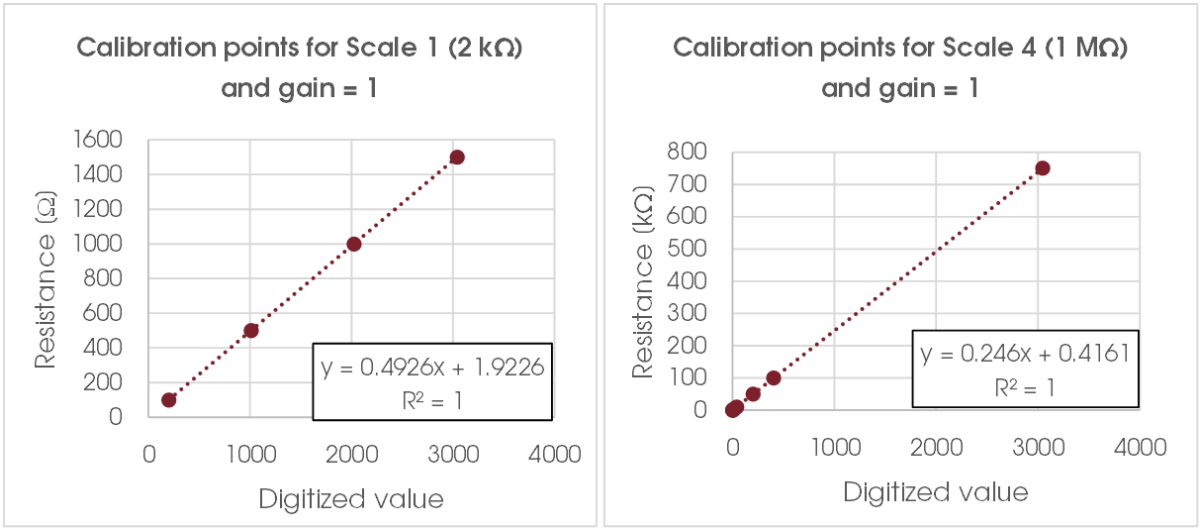

Figure 5.6: Measurements points and linear fit for two scales.

Chapter 6

Conclusions and future work

This chapter concludes this report, presenting conclusions about the developed work, as well as possible future developments.

6.1 Conclusions

The aim of this project was to develop a method and system that could identify faults in wiring prior to their happening.

This goal was achieved with the development of a sensor embedded into the cable and companion measurement system. The sensor uses two thin wires, one manganin wire and one copper wire, wrapped around the cable to be monitored and a set of precision SMD resistors were soldered to both wires, creating parallel elements. This further refines the method proposed by Active Space Technologies patent and, thus, the patent as being amended.

The defined requirements for this development have been achieved to prove the concept and functionality of the method and system. A sensor that can detect defects in the harness with a minimum diameter of 1 cm and a 1 m resolution was built. The range of the monitoring unit is 20 m, however it can be increased to 30 m or even 40 m given certain conditions. Moreover, a trade-off between size of the defect and total range to be monitored is possible. Other alternatives could consist in interlacing another sensor to the former, reducing the minimum defect size that could be detected to half. This would not increase the complexity of the measurement unit; both sensors could share, through multiplexing techniques, the same measurement channel. This method can be scaled using n sensors wrapped around the cable, hence reducing minimum defect size by a factor of n.

The developed sensor increases the mass of the cable to be monitored by 15%. The sensor costs approximately 0.75 € per meter, excluding outer insulation. These values could be reduced with mass production prices and manufacturing processes.

The sensor measurement capability withstood large temperature variations as well as induced noise, excluding the effects caused by the variation in resistivity of the glue

used to mount the resistors on the cable. However, this could be solved using a glue that maintains good electrical insulation even at high temperatures.

The companion measurement system has been fully characterized and behaves correctly. The system can measure the sensor resistance and determine whether if a fault is about to happen.

6.2 Future work

As this work presents a prove of concept approach, further developments can be made to reach a final commercial product. Most of these developments should focus on the manufacturability of the sensor and interference testing. Some of these developments could include:

- Find the diameter of the protective mesh that best characterizes the mechanical stress of the main conductor and built a test setup to reproduce faults in the sensor.
- Optimize the architecture for mass production.
- Additional testing of the sensor in adverse environment conditions, including temperature cycles and electromagnetic compatibility.
- Interface the sensor and measurement system to existing aircraft communication protocols.

References

[1] *Global Market Forecast - Future Journeys 2013-2032*, Airbus, 2013.

[2] D. Forsberg, *Aircraft Retirement Trends and Outlook*, Avolon, September 2012.

[3] *Aircraft Wiring Degradation Study*, U.S. Department of Transportation, January 2008.

[4] J. Morton, R. Nicholson, and B. Roberson, *Flight and Cabin Crew - Response to in-fligh smoke*, Boeing, April 2001.

[5] Wikipedia, "Transmission line — wikipedia, the free encyclopedia," 2015, [Online; accessed 28-February-2015]. [Online]. Available: http://en.wikipedia.org/w/index.php?title=Transmission_line&oldid=644771857

[6] *Time Domain Reflectometry Theory*, Agilent Technologies, Inc, May 2013.

[7] C. Furse, Y. Chung, C. L, and P. Pendayala, "A critical comparison of reflectometry methods for location of wiring faults," January 2006.

[8] *Understanding SAR ADCs: Their Architecture and Comparison with Other ADCs*, Maxim Integrated, October 2001.

[9] *ZigBee PRO Stack - User Guide*, NXP Laboratories UK, Ltd, May 2012.

[10] *Annual passenger total approaches 3 billion according to ICAO 2012 air transport results*, International Civil Aviation Organization, December 2012.

[11] C. Furse and R. Haupt, "Down to the wire," February 2001.

[12] *Transportation Statistics Annual Report 2012*, U.S. Department of Transportation, August 2013.

[13] *TWA800 - Aircraft Accident Report*, National Transportation Safety Board, July 1996.

[14] W. S. S. I. W. Group, *Review of Federal Programs for Wire System Safety*, National Science and Technology Council, November 2000.

[15] *SWR111 - Aviation Investigation Report*, Transportation Safety Board of Canada, September 1998.

[16] *Harness integrated sensors network for wiring health monitoring*, Active Space Technologies, April 2013.

[17] *Research and Technology Development Projects - 14th call, SP1-JTI-CS-2013-01*, Clean Sky, January 2013.

[18] A. Mendes and F. Simões, "Method and system for monitoring electrical wire aging," Patent PT106 994-A, 2013, pending.

[19] *Essential Elements of an Electric Cable Condition Monitoring Program*, United States Nuclear Regulatory Commission, April 2010.

[20] Z. Xu, S. Saha, D. Koltsov, A. Richardson, B. Honary, J. Hannu, A. Sutherland, B. Moffat, and M. Desmulliez, "Embedded health monitoring strategies for aircraft wiring systems," in *Electronics System-Integration Technology Conference, 2008. ESTC 2008. 2nd*, September 2008, pp. 463–470.

[21] Y. C. Chung, N. Amarnath, and C. Furse, "Capacitance and inductance sensor circuits for detecting the lengths of open- and short-circuited wires," *IEEE Transactions on Instrumentation and Measurement*, vol. 58, no. 8, pp. 2495–2502, August 2009.

[22] A. Siddoju, C. Gogineni, S. Bajjuri, and S. Sathish, "Embedded sensors to assist proper installation of wire harness clamps and to monitor degradation of wires," in *9th Joint FAA/DoD/NASA Conference on Aging Aircraft*, March 2006.

[23] *Standard prices list for all wires*, GoodFellow, September 2014.

[24] *Manganin - Data sheet*, IsabellenHutte, March 2014.

[25] F. Zandman and J. Szwarc, *Non-Linearity of Resistance/Temperature Characteristic: Its Influence on Performance of Precision Resistors*, Vishay Intertechnology, June 2009.

[26] W. Jung, *Op Amp Applications Handbook*. Elsevier.

[27] *REF31xx - 15ppm/°C Max, 100 μA, SOT23-3 Series Voltage Reference*, Texas Instruments, February 2006.

[28] *OPA330 - 50μV V_{OS}, 0.25μV/°C, 35μA CMOS Operational Amplifiers Zerø-Drift Series*, Texas Instruments, February 2011.

[29] *PMGD370XN*, Philips, February 2004.

[30] *MCP3201 - 2.7V 12-Bit A/D Converter with SPI Serial Interface*, Microchip, August 2006.

Appendix A

Test plan

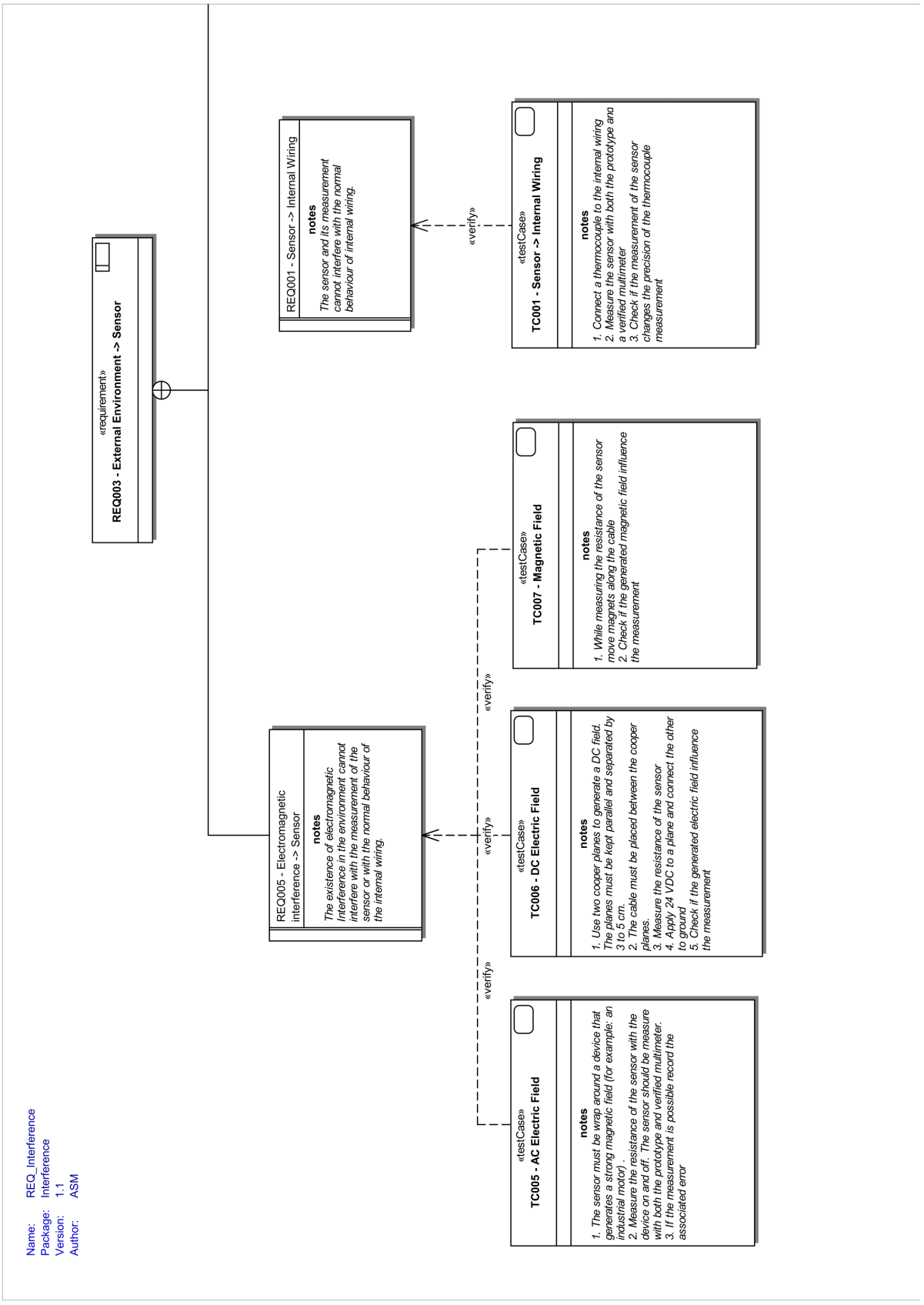

Figure A.1: Full specified test plan (Part 1).

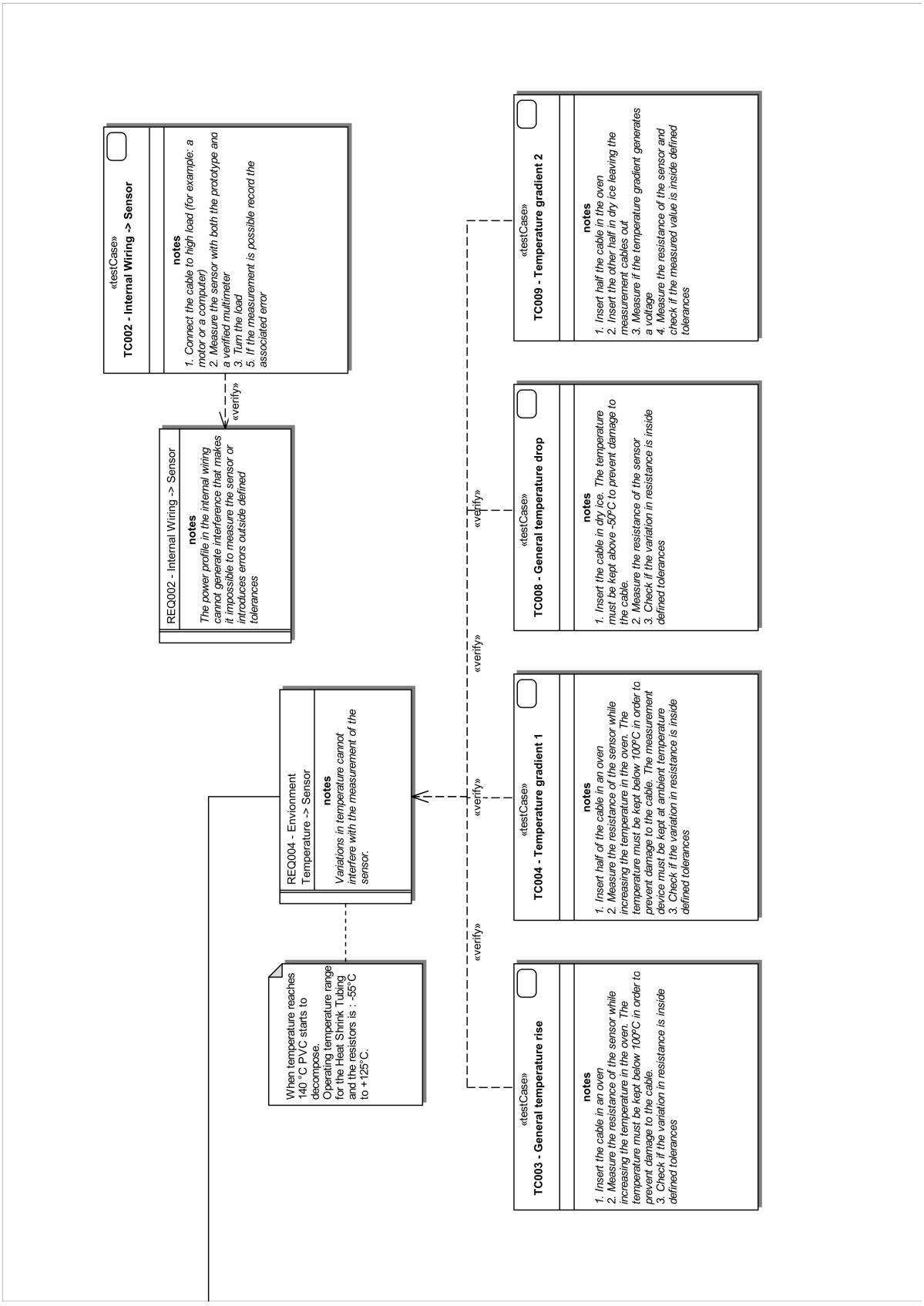

Figure A.2: Full specified test plan (Part 2).